Patterning planar surfaces with motor proteins: Towards spatial control over motile microtubules

Cordula Reuther

Von der Fakultät Maschinenwesen
der Technischen Universität Dresden
zur Verleihung des akademischen Grades
Doktor-Ingenieur
genehmigte Dissertation

Dresden 2009

Arbeit eingereicht am: 19.03.2009
Tag der mündlichen Prüfung: 11.06.2009

Betreuer: Dr. Stefan Diez
Gutachter: Prof. Dr. rer. nat. habil. Wolfgang Pompe
Prof. Dr. Henry Hess

Table of contents

List of abbreviations

2D	two-dimensional
AFM	atomic force microscope
AMPPNP	adenylyl-imidodiphosphate
ADP	adenosine diphosphate
ATP	adenosine triphosphate
BRB	Brinkley reassembly buffer
DNA	deoxyribonucleic acid
DPN	dip-pen nanolithography
EGTA	ethylene glycol-bis (2-aminoethylether)-N,N,N',N'-tetra acetic acid
FITC	fluorescein-5-isothiocyanate
GFP	green fluorescent protein
LCST	lower critical solution temperature
LHC	light-to-heat conversion
μcP	micro-contact printing
NA	numerical aperture
ncd	non-claret disjunctional
PDE	partial differential equation
PDMS	polydimethylsiloxane
PIPES	piperazine-N,N'-bis -(2-ethanesulfonic acid)
PNIPAM	poly(N-isopropylacrylamide)
UV	ultraviolet

1 Introduction

Cells can be viewed as tiny and complex factories in which each subcellular structure fulfills its very specific task but at the same time also communicates with its environment. These sophisticated biological machines possess a huge variety of capabilities including energy conversion and transduction, synthesis of specific organic chemicals, creation of biomass, information storage, recognition, signaling, sensing, self-assembly, and reproduction [1]. Moreover, there exist biomolecular analogues for many conventional devices, such as structural components, wires, motors, drive shafts, pipes, pumps, production lines, and programmable control systems [2]. Consequently, there is growing interest in mimicking biological processes for creating nanoscale devices, which promise savings in mass and energy consumption and operate with great precision and functionality [1, 3-7].

The abilities of natural molecular machines also stimulated the train of thought that led to the visionary concept of molecular manufacturing [2]. The anticipated technology wants to apply non-biological molecular machinery for the construction and manipulation of nanoscopic as well as of macroscopic objects from nanoscale building blocks. Unlike current 'top-down' approaches, where large devices are used to work from the macroscopic to the microscopic level, the proposed 'bottom up' concept aims to structure matter to complex atomic specifications. Unfortunately, the realization of this concept lies still ahead in the future because current technologies have so far been confined to two dimensions (2D). Thus, it will be crucial to develop entirely new approaches to the construction of three-dimensional nanoarchitectures.

Cellular machines are supposed to not only serve as inspiration for technological objectives but also to advance the tools and instruments available for molecular manufacturing [3, 5]. In particular biomolecular motors, which are able to efficiently convert chemical energy into controlled motion, could be exploited to engineer hybrid nanomechanical systems. Exemplarily, this was shown by integrating the rotary motor F1-ATPase into an engineered environment and employing it to propel a nickel bar [8].

Motors from the kinesin and myosin families transport cargo along filamentous tracks of the cytoskeleton (e.g. microtubules and actin filaments). As, so

far, no man-made motor smaller than 1 μm has been demonstrated to be capable of carrying load [4, 6], it is intriguing to apply such motor proteins for building nanoscale transport systems. These systems are envisioned to not only load, transport, and unload cargo but to be applied e.g. in sensors, sorters and actuators, for self-healing materials, and to miniaturize microelectromechanical systems (MEMS) [4, 9, 10]. However, in order to successfully implement them into engineered environments the confluence of scientific developments in molecular biology, materials science, chemistry and nanofabrication is essential.

In order to perform transport tasks in engineered environments motor proteins are most commonly attached to a substrate and the heads of the motors move filaments, which are used as transportation platforms, across the surface. Because this motion is random a main requirement for well-controlled transport is to spatially guide the filaments. Various techniques involving topographical surface structures have been proven to be quite efficient [11-16]. However, preparing such surfaces is labor-intensive and costly. Moreover, the layout of the filament pathways cannot be altered in-situ if necessary. Attempts to guide microtubules on flat, chemically patterned surfaces were not satisfactory so far [17, 18]. In those approaches it turned out that the angle with which the microtubule approached the edge of a track was a decisive factor [19]. Since the guiding efficiency was the highest for shallow approach angles, narrow tracks are supposed to be preferential. Thus, the technical capability of patterning motor proteins with high resolution is a prerequisite for guiding microtubules on chemically patterned surfaces. Moreover, other challenges for patterning proteins are to achieve specificity and to preserve the functionality of the motors. Although a number of techniques, as e.g. microcontact printing and dip-pen nanolithography, have been studied extensively for patterning proteins [20-24], including antibodies [25], their applicability for biomolecular motors has not been investigated. Patterning motor proteins on planar surfaces was so far only performed by plasma deposition of molecules, which resist protein adsorption, and applying the motors to the patterned surface [18, 19]. However, in these experiments the resolution of the motor tracks was in the micrometer-range and thus not sufficient for reliably guiding microtubules.

It was therefore the first goal of this work to establish a patterning method for generating nanometer–sized tracks of motor proteins and to characterize the ability of

these tracks for guiding microtubules on planar surfaces. This was achieved by using microtubules as biotemplates to specifically transfer and bind kinesin-1 molecules, respectively (chapter 3). The second major goal was to explore an in-situ patterning technique for motor proteins, which enables the user-defined design of motor patterns. Therefore, localized light-to-heat conversion was combined with a switchable polymer layer. This way the protein binding properties of the surface were altered and allowed local protein adhesion in the illuminated areas (chapter 4).

While this work mainly aims to contribute to the rapidly growing toolbox for harnessing the motility of biomolecular motors in technological applications, it is clear that only the successful integration of the individual approaches will eventually enable the assembly of complex functional nanodevices. In any case, the developed techniques shall provide new options for studying biological motors as well as for expanding the current understanding of their mechanisms.

2 Background

2.1 Microtubules and motors

Microtubules, 25 nm in diameter and several micrometer in length, form part of the cytoskeleton of all eukaryotic cells. They give structure and shape to a cell, and serve as tracks for motor proteins to move organelles through the cytoplasm. Moreover, microtubules are the major components of cilia and flagella, and participate in the formation of spindle fibers during cell division (mitosis). Microtubules are formed by self-assembly of tubulin. Each tubulin subunit is a heterodimer comprised of tightly linked globular α- and β-tubulin proteins. The subunits assemble in a head-to-tail fashion into protofilaments, which associate laterally with a small lengthwise shift to create stiff, hollow tubes (Fig. 1).

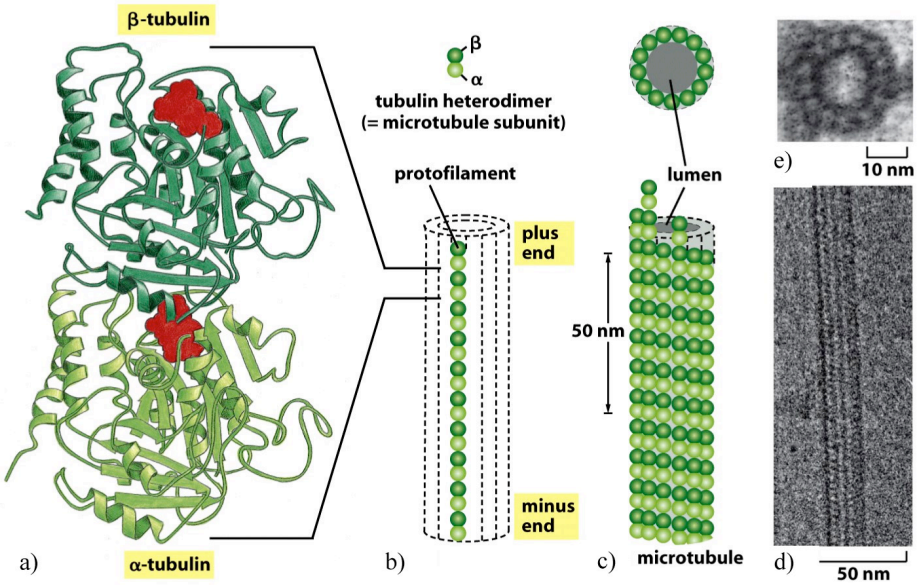

Figure 1: The structure of microtubules. a, The tubulin heterodimer is formed from a tightly linked pair of α- and β-tubulin monomers and **b,** assembles head-to-tail into protofilaments with α- and β-tubulin units exposed at the minus and the plus end, respectively. **c,** Hollow tubes, the microtubules, are formed by lateral association of the protofilaments. **d,** Electron micrograph of a microtubule segment and **e,** a microtubule cross section. Figure adapted from [26].

In vivo, microtubules usually comprise 13 protofilaments but can be also composed of any number of protofilaments between 8 and 20 [27]. Owing to the asymmetry of tubulin and its periodic arrangement in the lattice, the microtubule structure shows a structural polarity, with only α-tubulin proteins exposed at one end and only β-tubulin proteins at the other. Because the two ends of a microtubule are not the same, the rate at which growth or depolymerization occurs at each pole is different. The end of a polarized filament that grows and shrinks the fastest is known as the plus end and the opposing end is called the minus end. For microtubules, the minus end is the one with exposed alpha-tubulins. In a cell, it is this end that is located at the centriole-containing centrosome found near the nucleus, while the plus end, comprised of exposed beta-units, is projected out toward the cell's periphery. Because microtubules constantly polymerize and depolymerize they are usually stabilized for *in vitro* applications. The antimitotic drug paclitaxel (also brand-named taxol), extracted from the bark of yew trees, for example, binds tightly to the microtubules and suppresses the exchange of tubulin subunits. [26, 28]

Linear motor proteins, like kinesins, dyneins or myosins, move along intracellular filaments of the cytosceleton, and thereby they generate force. Their motion is driven by the hydrolysis of adenosine triphosphate (ATP) with the general mechanism being ATP binding to a motor domain, hydrolyzation of ATP to adenosine diphosphate (ADP) and inorganic phosphate (P_i,) and releasing ADP and P_i. This leads to a 'powerstroke' against load. The variations of speeds and step-sizes found in motor proteins result from differences in rate-constants for the reaction steps and different morphologies.

The microtubule motor kinesin-1 was the first motor of the kinesin-family to be identified [29, 30] and has been most intensively studied. The kinesin-1 molecule is a homodimer of two heavy chains, each of which possesses an amino-terminal motor domain ('head'), a 60 to 80 nm long stalk with alternating flexible and coiled-coil segments, and a carboxyl-terminal small globular tail domain (Fig. 2). The neck, which joins the stalk to the motor domains, consists of the end of the coiled-coil stalk and two neck-linkers. Kinesin-1 is mainly involved in the transport of organelles and vesicles. One single molecule of this motor is capable of processive movement over move many steps without dissociating from the microtubule [31-34]. Thus, at least one head remains always attached to the microtubule during the cyclic motor reaction.

The two motor domains are thought to alternately bind to the microtubule in a hand-over-hand fashion [35-38] facilitated by a change in the affinity of the motor domain to the microtubule due to a small conformational change during the hydrolysis cycle. For each ATP hydrolyzed, kinesin-1 takes an 8 nm step on the microtubule lattice [39-41], a distance corresponding to the size of one tubulin dimer. Kinesin-1 thereby follows the protofilament axis with great fidelity [42, 43] towards the plus end of the microtubule. The velocity generated *in vitro* is typically between 0.6 and 0.8 μm/s [44, 45] (at ambient temperature) and the force about 6 pN [46-48].

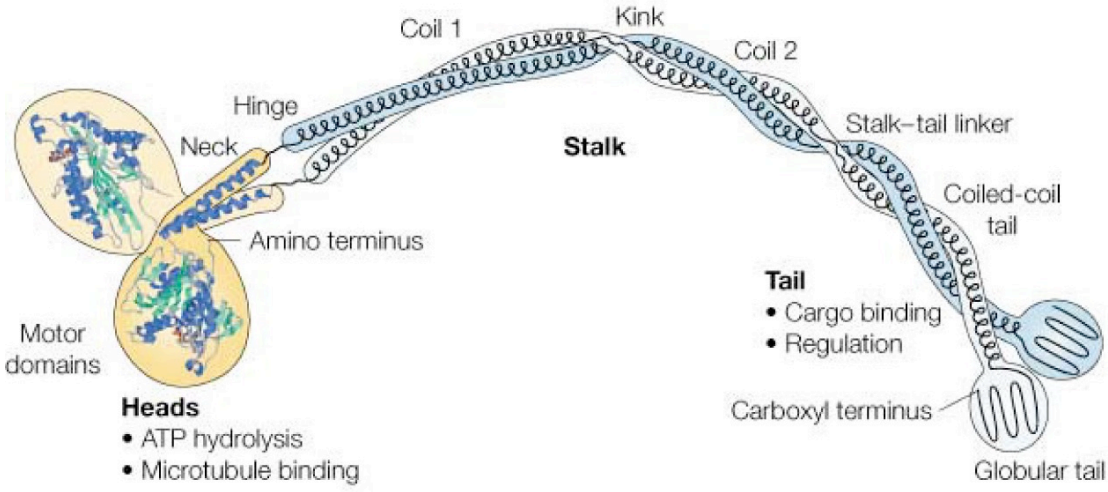

Figure 2: The structure of the kinesin-1 heavy-chain dimer. The image shows the crystal structure of the catalytic domains and the neck as well as the structure of the stalk and the tail as inferred from electron microscopic images and coiled-coil prediction analyses. Figure adapted from [49].

Non-claret disjunctional (ncd), a dimeric member of the kinesin-14 family, was discovered in 1990 [50, 51]. Ncd is involved in mitosis [52, 53] and meiosis [54, 55] where it is assumed to participate in spindle assembly and in modulating the spindle length. In contrast to kinesin-1, ncd is comprised of a carboxyl-terminal ATP-hydrolyzing motor domain as well as an amino-terminal ATP independent binding site [56, 57]. The neck consists only of the end of the coiled-coil stalk and is tightly associated with the two heads [58]. This alteration in the head-neck interaction, compared to kinesin-1, is thought to cause the minus-end directionality of ncd [49, 59-63]. The speed by which ncd translocates along a microtubule *in vitro* is only about 160 nm/s (at ambient temperature) [56, 64]. Moreover, although a recent study

reported processive runs of ncd *in vitro* under low salt conditions [65], the motor is usually been considered to be non-processive [66, 67].

Dyneins are another group of microtubule motors that can be divided into cytoplasmic and axonemal dyneins. Cytoplasmic dyneins are found in all animal cells, and perform a variety of fundamental cellular functions including organelle transport, assembly of the mitotic spindle, and nuclear migration. Axonemal dyneins cause the bending of microtubules in axonemes and thus produce the beating that propagates cilia and flagella. Axonemal dynein was already discovered in 1965 [68]. However, because of its large size (in the range of 1 MDa) and the difficulty of producing mutants, dyneins are still less characterized than kinesins. Axonemal dynein motors either contain one, two or three non-identical heavy chains (depending on the organism and location in the cilium). The *Tetrahymena* ciliary 22S dynein, derived from the outer arms of ciliary axonemes, comprises three different heavy chains (> 500 kDa). Each of these heavy chains is composed of a carboxyl-terminal globular head together with a coiled coil stalk that carries the microtubule binding site at its tip, and an amino-terminal tail (cargo binding domain) [69]. The motor domain consists of six AAA (ATPases associated with diverse cellular activities) domains and a seventh domain, which form an asymmetric ring. The first AAA domain is responsible for dynein motility. 22S dynein moves towards the microtubule minus-end, and translocates microtubules *in vitro* at a velocity of 8 µm/s [70]. Further, it was reported that 22S dynein moves processively with 8 nm steps at low ATP concentrations (< 20 µM) [71].

2.2 Molecular transport in synthetic environments

The sophisticated design of biomolecular motors, which outperforms any currently known man-made motor, has been inspiring. These tiny, nanometer-sized machines fulfill their very diverse tasks in biological systems with high specificity. They are involved in self-assembly as well as in active transport processes, where limitations of diffusion are overcome. Biomolecular motors directly convert chemical energy into mechanical motion whereat they achieve energy efficiencies of 50 % [28, 45] and more [72]. Moreover, they operate in a highly parallel manner and can generate large forces when acting cooperatively. Therefore it has been proposed, and many steps have already been taken, to exploit the outstanding characteristics of biomoleclar

motors for nanomanufacturing and the development of hybrid organic-inorganic nanodevices.

Towards this goal, biomolecular motors have to be implemented into engineered environments. Thereby it is advantageous that the motors can be produced conveniently and inexpensively by bacterial expression in *E. coli*. Through genetic engineering they can be modified to the intended function. Moreover, the motors are relatively robust as they withstand temperatures in the range of 5 to 45°C, pH values from 6 to 9, and ionic strengths from 50 mM to 300 mM [45]. Nevertheless, there are also limitations in using biomolecular motors due to them operating only in aqueous environments similar to the cytosol and due to the need of avoiding denaturing substances. Another important aspect is protein adsorption to a solid surface. Protein-surface interactions are determined by the physical state of the material, protein properties, and solution environment. All these factors play a major role in maintaining the protein activity. It is thus not always straightforward e.g. to substitute proteins buffers or substrates within a working assay.

Efforts to utilize molecular motors for cargo transportation in nanotechnology are based on so-called *in vitro* motility assays, which have played an important role in determining most of the motors' key properties described in the previous chapter. These assays are biological test systems where the action of motor-filament systems can be studied on an artificial surface outside the cell allowing controlled chemical conditions and the use of protein engineering. The motility is usually observed under the light microscope using fluorescence markers or high-resolution brightfield techniques. Based on their geometry two basic types of motility assays can be distinguished: the stepping assay and the gliding assay (Fig. 3).

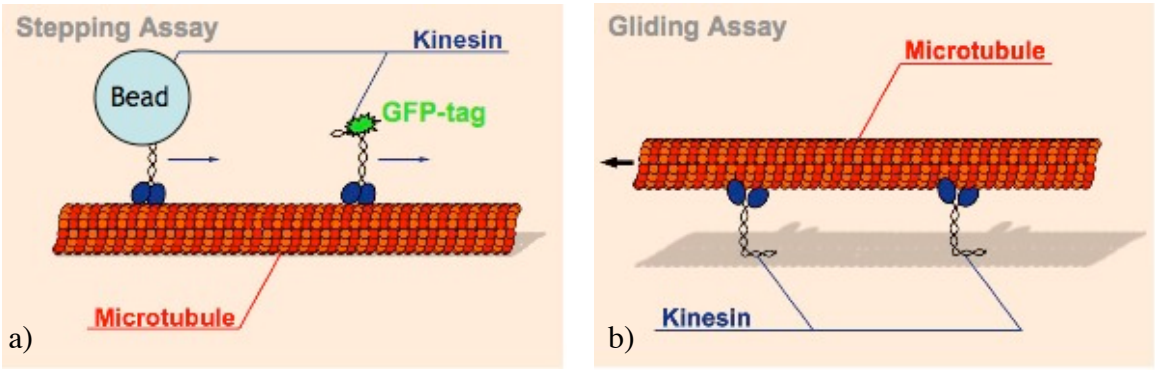

Figure 3: *In vitro* motility assays. a, In a stepping assay microtubules are immobilized on the substrate. Motors diffusing in solution may bind to a microtubule and move unidirectionally on its lattice. In order to easily observe the motor action they can be e.g. coupled to a bead or labeled with a fluorescent marker. **b,** In a gliding assay motor proteins are immobilized on the substrate. Microtubules bind to the exposed motor domains when being in close proximity to the surface. The motors then transport the microtubules across the surface with, in the case of kinesin-1, the minus end leading.

The stepping assay closely mimics the cellular system: Cargo is transported along a surface-immobilized filament by the motor. Using this assay micron-sized glass particles [73], silicon microchips [74], and quantum dots [75] have been transported by kinesin-1 motors on immobilized microtubules. Further, oriented microtubule networks have been shown to allow directed cargo-transport [73, 76, 77]. Such unidirectional motility can be preferential and might enable the simultaneous application of different motors. However, it is not possible to further control the motility, e.g. change the moving direction. Moreover, to ensure that motor-linked cargo does not dissociate from its track after having walked distances of typically 1 μm (the processivity length of kinesin-1) [78, 79] the cargo has to be coupled to several motors for reliable long-distance transport.

In the gliding assay the geometry is inverted so that the motors are fixed to the substrate and microtubules glide over the assembly. Here, cargo can be coupled to the microtubule shuttles using the biotin-streptavidin linkage or antibodies. At a sufficient density of surface-immobilized motors, multiple motors attach to a single microtubule and ensure that it continues to glide despite the detaching of single motors. The gliding geometry is usually favored for setting-up nanotransport systems (Fig. 4), where cargo is to be shuttled between defined locations in a controlled manner.

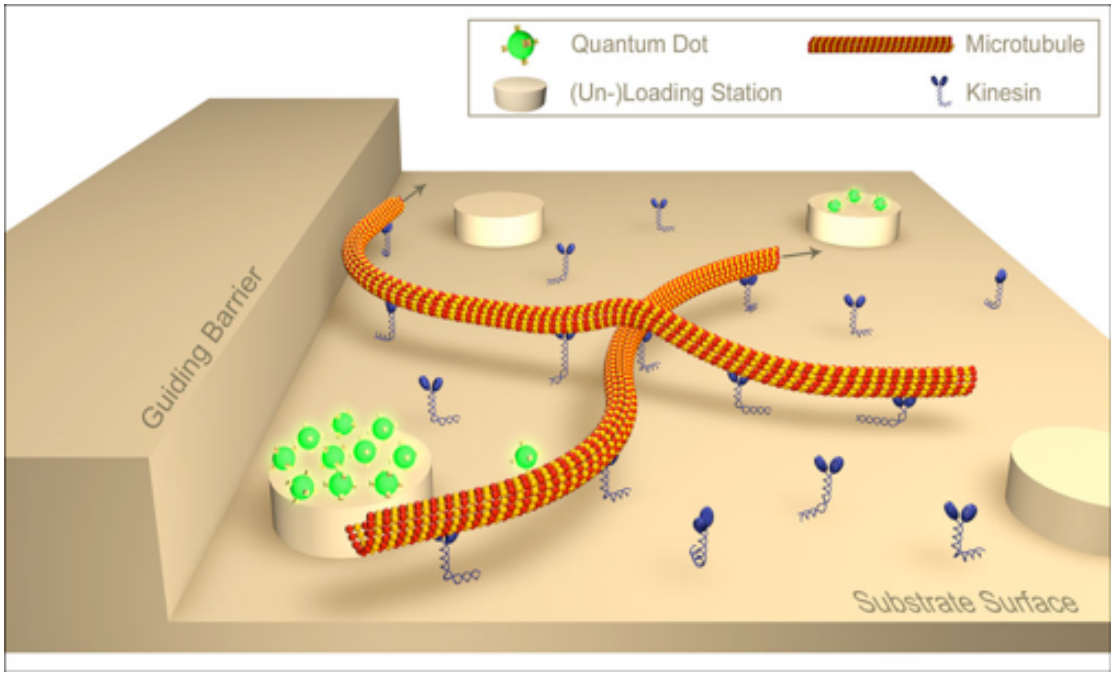

Figure 4: Schematic illustration of a nanotransport system based on molecular motors. At defined loading stations cargo (e.g. quantum dots) are picked up and specifically bound to microtubule-shuttles, which are propelled by surface-attached kinesin motors. The microtubule is thereby directed towards defined unloading stations, where the cargo is to be delivered.

These nanotransport systems are envisioned for applications like molecular sorting, sensing, separating, concentrating, or self-assembly [9, 10, 80]. So far, a number of active transport tasks could be performed using the kinesin-1-microtubule system. These include stretching of deoxyribonucleic acid (DNA) molecules [81, 82], probing receptor-ligand interactions [83] or surface topography [84], transport of biological or engineered cargo [81, 85-87], cargo loading out of solution [88] or pick-up from loading stations [89], concentrating of proteins [90], as well as molecular sorting [91]. Additionally aspects influencing the design of transport systems were studied, e.g. the distance above which microtubules glide above the surface [92], or the effects of microtubule rotation around their longitudinal axis during cargo transport [93].

The main challenge for organized nanotransport is the temporal and spatial control of motility. Reversibly switching microtubule motion on and off can be achieved by ATP regulation. With the help of a microperfusion system ATP in the flow-cell was rapidly exchanged with the non-hydrolyzable ATP analog adenylyl-

imidodiphosphate (AMPPNP) to start and stop motility [94]. Another approach used caged ATP to locally start motility upon exposure to ultraviolet (UV) light [87, 95]. Active steering of microtubules was demonstrated by using external electric [91], magnetic [96], or hydrodynamic flow fields [94, 97]. Besides that, spatial guiding was also accomplished without external control. In contrast to the random motion in a basic gliding assay, guiding of microtubules was first achieved by topographical grooves or channels on the substrate surface [98-100]. Here, microtubules were directed along a path by the channel walls that forced them to stay on the bottom of the channels. This method was enhanced by combining topography and chemical surface modifications [11, 15] to prevent microtubules from "climbing up" channel walls and changing tracks. Advancements in the channel geometry [12, 14], like overhanging walls [13], further improved the guiding performance enabling reliable long-distance transport. Asymmetric channel features and arrowheads were used to control the direction in which microtubule shuttles were guided [16].

The kinesin-1-microtubule system has most often been favored over myosin-actin as cargo carrier system [10, 74] because the high bending rigidity of microtubules reduces their chance of turning around. The maximum width of guiding channels can be larger and fabrication is more facile. However, the actomyosin motor system might become more attractive in future since flexible filaments allow smaller turning radii and potentially a further miniaturization of motor-powered devices [101, 102]. In addition, transportation by myosin is up to 10 times faster than by kinesin-1. Possibly, combining both motor systems might open up new possibilities of realizing complementary tasks in parallel.

2.3 Guiding on planar surfaces

Though filaments can be efficiently guided through combined topographical and chemical methods, as described in the previous chapter, fabrication of the necessary structures is labor-intensive and costly. Additionally there are potential applications in which static topographical features might be disadvantageous, such as transport of cargo with diameters larger than the channel dimensions.

Chemical patterning of planar surfaces can also restrict movement of filaments to areas with high motor densities. However, at a boundary to lower or zero motor

density walking off of filaments cannot be prevented [17, 18]. Guiding of microtubules at such a chemical boundary is only due to thermal fluctuations. If a microtubule crosses the boundary its tip becomes free to fluctuate (Fig. 5a). The microtubule is then only guided when the thermal energy ($kT/2$, where k is the Boltzmann constant, and T is the temperature) required for overcoming its flexural rigidity (EI, where E is the modulus of elasticity, and I the geometric moment of the beam cross-section) and for bending back onto the motor track is sufficient. Otherwise the microtubule will be propelled in a straight line by the motors still in contact until it detaches. Only short microtubules can be reoriented through rotational diffusion around the last motor [17].

Aside from the flexural rigidity of the microtubule the amount of bending depends also on the average time that a microtubule free tip takes to deflect a given distance. This parameter can be described by the first passage time t_k. The equation for the first passage time of a fluctuating microtubule was derived by Clemmens et al. [19] as follows,

$$t_k = \frac{\gamma}{EI}\left(\frac{2L}{3\pi}\right)^4 \sqrt{\frac{\pi}{4}}\sqrt{\frac{kT}{2EI}\frac{L}{\tan^2\theta}}\exp\left(\frac{2EI}{kT}\frac{\tan^2\theta}{L}\right). \qquad \text{(Equation 1)}$$

Thereby, γ is the perpendicular drag coefficient, L is the overhang length of the fluctuating microtubule and θ is the approach angle. According to this equation the time needed for thermal fluctuations to bend a microtubule by an angle θ will increase radically as the approach angle θ increases. The time a microtubule has to sample the surface is limited by the time before it completely detaches from the track. This in turn depends on the gliding speed and the microtubule length. Thus, the probability for microtubule guiding should be the highest for shallow approach angles to the chemical edge. For small approach angles, the free microtubule tip needs only very slight bending and samples a sufficient area for finding the next motor. This was experimentally proven by Clemmens et al. [19] (Fig. 5b).

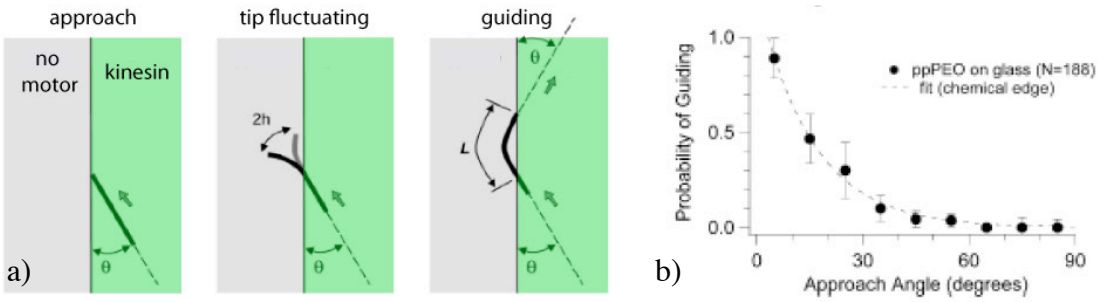

Figure 5: Guiding at a chemical boundary. a, Schematic of microtubule guiding due to bending at a chemical boundary. A microtubule is driven towards a chemical boundary under an approach angle θ. As the microtubule tip is not longer attached to motors it begins to fluctuate with h being the tip displacement. If the overhanging microtubule (with L being the overhang length) can be bent far enough to attach to a motor on the track, it will continue gliding. **b,** Probability of microtubule guiding for different approach angles at a chemical boundary. Figure adapted from [19].

In order to achieve effective guiding on patterned planar surfaces it can be assumed that motors arranged in straight narrow tracks restrict aligned microtubules to shallow approach angles. The width of the tracks should be less than 1 µm. However, as this feature size is still much larger than the 25 nm diameter of a microtubule, and defines the orientation of short filaments poorly [4], a track width of only a few hundred nanometers would be ideal. Within this work methods of creating such narrow motor tracks are investigated and the reliability of microtubule guiding and motility on such chemically patterned surfaces is studied (see chapter 3).

2.4 Surface patterning of proteins

Surface patterning of proteins is of interest in a wide number of applications. These include biosensors, diagnostic immunoassays, cell culturing, DNA microarrays, and other analytical procedures [103-110]. Thereby, the main challenges are: controlling protein orientation, preserving biological activity of the proteins, achieving high resolution as well as patterning different proteins. Moreover, it is desirable that the technique is flexible, inexpensive, and offers the potential for high through-put production. The specific patterning requirements may, however, depend very much on the application.

Generally, one can distinguish two protein-patterning strategies: indirect methods and active placement. In indirect methods, a surface is pre-patterned for enhanced protein binding in some parts of the surface along with largely reduced adsorption on the rest of the surface. On the other hand, direct patterning (i.e. active placement) is often more specific and more facile than indirect patterning. However, the risk to fully or partially denature the protein is usually higher, e.g. due to adsorbing the proteins to a stamp or illuminating the protein solution with UV-light. In the following different patterning techniques are shortly introduced and discussed with respect to the patterning of motor proteins.

Microcontact printing (μcP) is a simple and efficient soft-lithographic patterning technique for proteins [20, 21]. It uses a polydimethylsiloxane (PDMS) stamp to deposit molecules on surfaces and was originally developed by Whitesides and coworkers [111] for self-assembling alkanethiols on gold substrates with spatial control. The stamp is first 'inked' with a solution of molecules that coat the stamp. The stamp is dried and pressed onto the surface to be patterned. The soft PDMS stamp makes conformal contact with the surface and molecules are transferred directly from the stamp to the surface. Repeated printing using different stamps can be used to make complex surface patterns of more than one kind of molecule. The stamps for microcontact printing are made using structured silicon wafers. The wafers form part of a mould in which liquid PDMS is polymerized. On demoulding, a flexible transparent stamp is obtained, with structures that can be in the submicron range [112, 113].

Dip-pen nanolithography (DPN) is a scanning probe lithography technique first demonstrated by Mirkin and coworkers in 1999 [114]. It uses an atomic force microscope (AFM) to pattern molecules on specific areas of a surface and is most commonly used to pattern self-assembled monolayers of long chain alkane thiols on Au surfaces. However, it has also been used to immobilize biomolecules such as proteins [22-24], DNA [115], and single viruses [116] with indirect and direct write methods. The tip of an AFM cantilever acts thereby as a "pen", which is dipped into a protein solution acting as an ‘ink’. When put in contact with a substrate (the ‘paper’) molecules are transferred via the solvent meniscus. This technique allows surface patterning in the 100 nm range and below. Recently, parallel patterning using multiple-pen cantilever arrays has also been demonstrated [117].

Another **AFM based nanolithography technique** employs a novel vibrational AFM mode (contact oscillation) to pattern even fragile proteins under native conditions [118]. On self-assembled monolayers and polymer-brush interfaces immobilized proteins can be detached with an AFM tip and replaced by other proteins, which are selectively self-assembled from the bulk. Thus, this method enables reversible in-situ patterning (write-read-erase) of self-assembled protein monolayers at dimensions down to 50 nm.

Last but not least, a variety of **photoimmobilization strategies** have been developed for producing protein patterns [119]. Several approaches work by photochemically modifying surfaces to promote or deter non-specific protein adsorption [120, 121] whereas others use photoactive particles, which link specific proteins to the surface [122, 123]. Unfortunately, all of these methods require the use of UV-light, which can be harmful for biological species [124]. Additionally many small molecule crosslinkers have to be spun on the substrate and dried before irradiation. A first approach of patterning in aqueous solution with longer and less damaging wavelengths was reported by Holden et al. [125]. They exposed a bovine serum albumin passivated surface through a photomask. Organic fluorophores in the buffer solution that had been covalently attached to ligands were excited on resonance causing photobleaching and attachment to the substrate via a mechanism involving singlet oxygen. More than one species could be patterned from a single solution if they were tagged with different fluorescent dyes and exposed sequentially by different wavelengths. The achieved pattern size was still in the micrometer range but could possibly be improved by employing a more collimated light source.

The applicability of the described techniques for patterning motor proteins will be discussed in the following. Kinesin-1 and other motors are quite sensitive proteins. Patterning them by direct microcontact printing most likely severely damages their biological functionality primarily due to the drying step on the elastomeric stamp surface. Moreover, the transfer by printing requires that the adhesion of protein to the substrate has to be stronger than that of the stamp. The 'sandwiching' of the proteins between surfaces of very different hydrophilic / hydrophobic properties might create a mechanical stress on the protein and lead to irreversible conformational changes [25, 126]. Although direct μcP of myosin motors for the guided elongation of actin filaments was shown recently [127], indirect

approaches should be generally more appropriate to assure a high density of active motors. In experiments in the run-up of this work it was managed to create 1 μm wide kinesin-1 lines by printing anti-Penta-His antibodies, blocking the rest of the surface, and finally binding his-tagged kinesin-1 to the patterned antibodies. The lines, however, did not prove to reliably guide microtubules mainly because the active motor density was too low.

Patterning of motor proteins using DPN has not been reported yet. Direct DPN patterning could principally be promising because the proteins do not have to be dried. However, so far even for patterning biologically active antibodies [128] an indirect approach proved to be more advantageous. In order to optimize the antibody orientation and to minimize denaturation, surfaces were pretreated with protein A/G, which was covalently attached to patterns of DPN-generated esters on gold surfaces.

AFM based nanolithography as well as photopatterning methods have not been used so far for patterning motors but might be an interesting alternative maybe also for directly patterning.

2.5 Switchable polymers

Switchable polymers undergo a sharp physical change when external stimuli are presented. Depending on the polymer the stimuli can be thermal, optical, electrical or electrochemical. Due to their ability to undergo such changes under easily controlled conditions these polymers are also classified as smart materials. There has been extensive research in exploiting the physical changes for various applications. Among them are nanoscale actuation [129], fluid manipulations in microfluidic devices [130], cell and protein adhesion [131-133], drug delivery [134], sensor applications as well as materials assembly and reconfiguration [135].

One numerously studied switchable polymer is the temperature-responsive poly(N-isopropylacrylamide) (PNIPAM). The first reports to recognise that PNIPAM displayed a phase transition was that of Scarpa et al. in 1967 [136] and Heskins and Guillet in 1968 [137]: both groups observed that PNIPAM became less soluble upon heating and formed a precipitate at about 32°C, the lower critical solution temperature (LCST). The LCST is based on specific interactions between the solute and the solvent. Below the LCST PNIPAM is water soluble. Its hydrophobic side groups hydrate through hydrophobic association of water molecules and the polymer chains

assume a swollen, hydrophilic state. Above the transition temperature the water is expelled and the polymer collapses because intra- and intermolecular hydrogen bonding of the polymer molecules are favored compared to a solubilization by water (hydrophobic state). Thermodynamics can explain this with a balance between entropic effects due to the dissolution process itself and due to the ordered state of water molecules in the vicinity of the polymer. Enthalpic effects are due to the balance between intra- and intermolecular forces and due to solvation, e.g. hydrogen bonding and hydrophobic interaction [138, 139]. Furthermore, it has been experimentally proven that the LCST behavior in polymers is governed by the hydrophobic to hydrophilic balance within the macromolecule [140-143]. The LCST can thus be modified through copolymerization of various amounts of hydrophobic or hydrophilic monomer units. In response to the change of the hydration state, the volume occupied by the polymer reversibly changes by up to an order of magnitude [144, 145]. The water molecules that surround the polymer below the transition temperature generate a repulsive hydration force that repels biological materials. In contrast, above the transition temperature the protective sheath of water is disrupted, allowing proteins to stick to the surface. The change of some key properties is depicted in Figure 6.

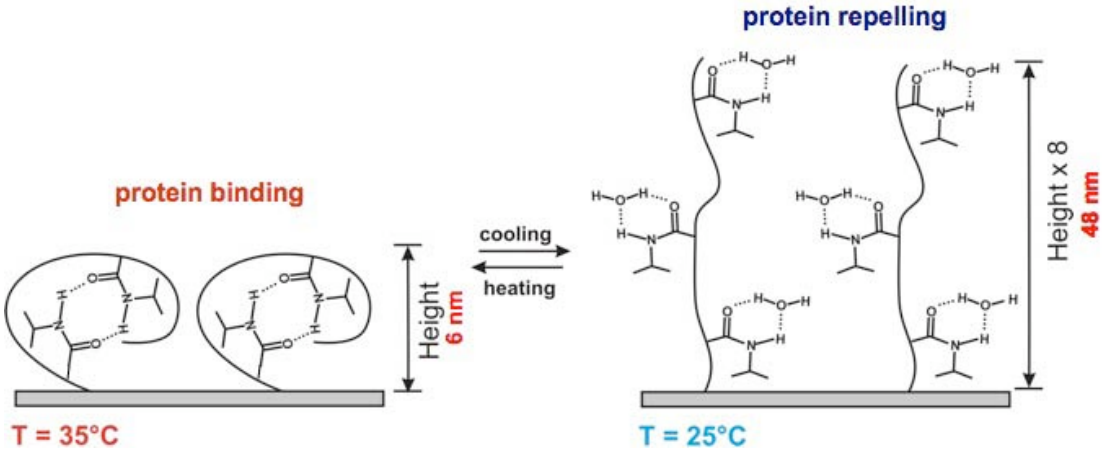

Figure 6: Temperature-dependent conformation of PNIPAM molecules. The surface-grafted PNIPAM chains reversibly switch their conformation upon cooling and heating. At temperatures above the LCST (of about 32°C) the molecule is collapsed and the surface becomes hydrophobic. In this state proteins are able to bind to the substrate. In contrast, below the LCST proteins are repelled because the polymer assumes a swollen, hydrophilic state. In conjunction with the conformational change, the height of the PNIPAM layer is also changed.

In order to use PNIPAM molecules for switching surface properties and for tuning protein adsorption, the polymer chains have to be organized in structures with some directionality. This is achieved in polymer brushes: densely grafted polymer chains that are covalently tethered with one end to the surface. Linear polymer chains grafted on the surface are gaining a brush like conformation if the distance of the chains is becoming smaller than twice the radius of gyration of the molecules. In this case the polymer chains assume a conformation stretched away from the surface due to excluded volume effects. The behavior of those ultrathin polymeric layers is strongly dependent on the grafting density, the molecular weight and the chemical composition of the polymer chains.

Brushes can be fabricated by 'grafting to' (tethering of polymer chains to a surface from solution) and 'grafting from' (radical polymerisation at the surface) methods. Dense polymer brushes are obtained via surface-initiated polymerization from initiator-modified surfaces, using a range of controlled radical, ring-opening, or methathesis polymerizations. These methods yield excellent control over brush composition and thickness [146]. Especially surface-initiated atom transfer radical polymerization (ATRP) is a suitable method for the controlled preparation of polymer brushes covalently bound to the surface of different substrates [147]. The control results from the use of a transition metal based catalyst. It is important to note that the LCST of PNIPAM grafted from the surface of solid substrates [148], cross-linked hydrogels [149], and block polymers [150] was reported to be nearly identical to the LCST of a homopolymer in aqueous solution.

Recently, kinesin-1-driven microtubule motility experiments have been successfully performed on polymeric brush layers. It was demonstrated that on polymeric gradient surfaces (grafting density gradient) gliding microtubules are sorted according to their length [151]. This was the first example of self-organized sorting of protein assemblies on surfaces. Moreover, motility can also be dynamically controlled by external stimuli [152]. Thereby, kinesin-1 molecules were adsorbed onto a substrate between surface-grafted PNIPAM chains. Reversible landing, gliding, and releasing of microtubules was then observed in response to temperature-induced conformational changes of the polymer. Another report showed that the size of bioactive kinesin-1 patterns can be controlled via temperature on surfaces containing lateral LCST gradients due to opposing gradients of hydrophilic and hydrophobic PNIPAM copolymers [153].

3 Biotemplated patterning of motor proteins

In this chapter the generation, characterization and application of nanometer-wide, non-topographical tracks of motor proteins is reported.

First of all, it was explored whether the regular lattice of reconstituted microtubules can be used as template structure to specifically bind and transfer kinesin-1 and ncd motor proteins on planar surfaces. Such an approach has the advantage that structurally oriented arrays of biomolecular motors can be generated. Throughout the whole process the motors remain in an aqueous environment and, in case of transferring, do not need to be adsorbed to an additional surface as in other direct protein patterning techniques. Thus, the biological activity of the motors is preserved.

In particular, two different methods of biotemplated patterning of planar surfaces with motor proteins were investigated: 'biotemplated stamping' (Fig. 7a) and 'biotemplated binding' (Fig. 7b). In the stamping approach, kinesin-1 molecules are bound in solution with their motor domains to 'template' microtubules in the absence of ATP. The generated complexes are then adsorbed onto the surface (step I), and ATP is added in order to propel the template microtubules off the surface-bound motor proteins. This way, tracks of oriented motor molecules, with their motor domains pointing away from the surface, can be generated (step II). In the binding approach, the template microtubules are first immobilized on the surface (step I). Kinesin-1 or ncd motor proteins are then specifically bound to the template microtubules via specific linker molecules or the second microtubule binding site in their tail domain, respectively (step II). In both approaches, either based on biotemplated stamping or binding, 'transport' microtubules in a motility solution containing ATP are added and glide along the patterned motor tracks (step III).

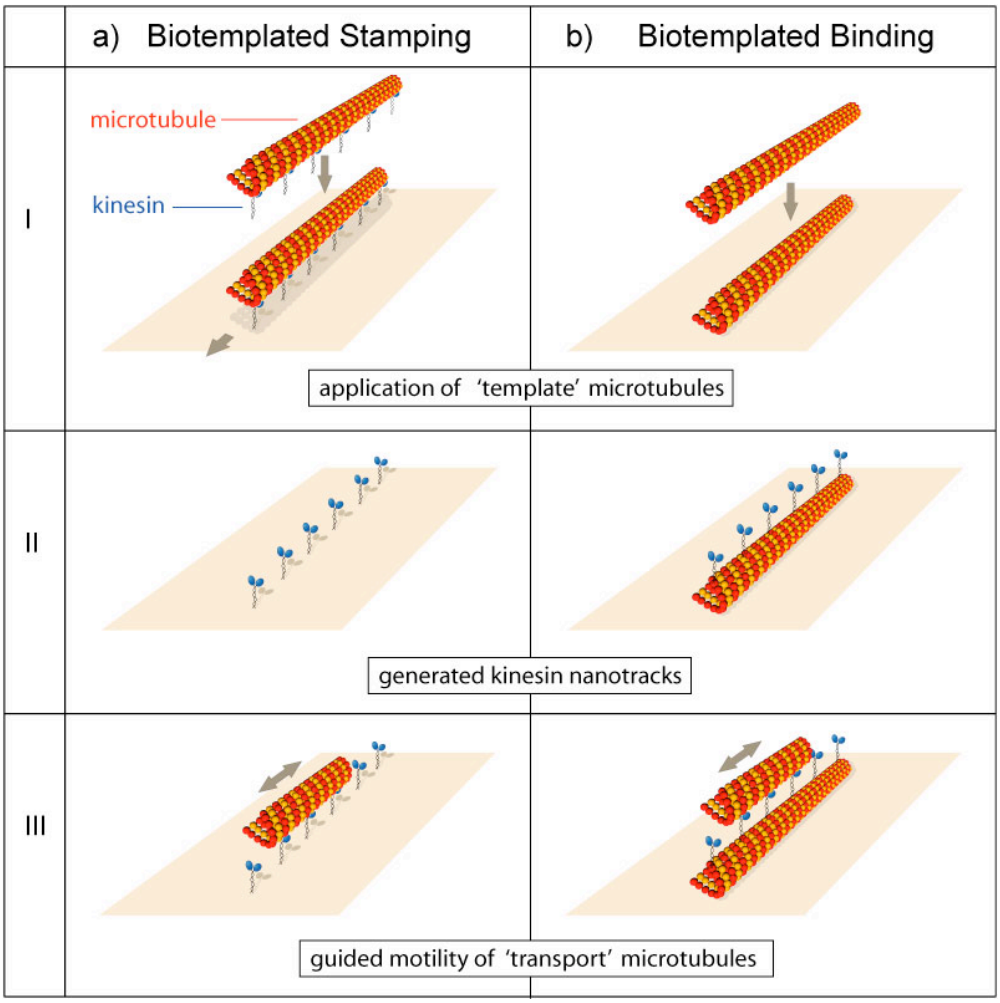

Figure 7: Methods of biotemplated patterning. a, Biotemplated stamping: Kinesin-1 molecules, which are bound in an oriented manner to the lattice of a template microtubule are transferred onto the surface by a stamping process (I). After adsorption the 'template' microtubule is released when the deposited motor molecules propel the microtubule off the generated track in the presence of ATP (II). The same molecules will move and guide the 'transport' microtubules (III). **b,** Biotemplated binding: Motor proteins are bound to a 'template' microtubule that was previously immobilized on the surface (I and II). 'Transport' microtubules then move specifically on the motor track, thereby sliding along the 'template' microtubule (III).

The movement of microtubules on the motor tracks was then studied with respect to guiding reliability as well as transport direction and velocity. Further, the width of the tracks was estimated. Finally, potential applications of such motor tracks for cargo transport and biophysical studies were explored, respectively.

The results of biotemplated patterning, presented in chapter 3.1 and 3.2, are published in [154].

3.1 Biotemplated stamping of kinesin-1

Within the work of establishing biotemplated stamping as a method for patterning kinesin-1 molecules a number of challenges had to be met. First, in order to exclusively transfer template-bound kinesin-1 molecules onto a surface and prevent random motility, free molecules had to be eliminated from the stamping solution. This could be accomplished by centrifuging the solution. However, the procedure and conditions of the process had to be optimized to avoid shortening of microtubules due to breakage and microtubule clustering. Secondly, the maximal possible kinesin-1 density on the 'template' microtubules was limited due to clustering of kinesin-1-microtubule complexes at higher motor densities. Clustering was also observed when binding dimeric one-headed kinesin-1 or other modified kinesin-1-constructs to templates. Increasing the ionic strength reduced clustering but at the same time also decreased motor-microtubule interaction and could thus not improve the kinesin-1 density on the 'template' microtubules. The reason for clustering was not elucidated but might be connected to interactions of the positively charged neck of the kinesin-1 molecule with the carboxyl terminus of tubulin [155].

In order to estimate the density of kinesin-1 molecules loaded to 'template' microtubules in solution kinesin-1 labeled with green fluorescent protein (GFP) was used for decoration. The fluorescent intensity of the loaded microtubules was compared to microtubules, which were bound to an anti-tubulin antibody coated surface and loaded inside the flow-cell with increasing GFP-kinesin-1 concentrations. Since in the latter case microtubules were immobilized, microtubule clustering was prevented even for high kinesin-1 concentrations. The fluorescent intensity of microtubules loaded with kinesin-1 molecules in solution without clustering equaled about the intensity of surface-immobilized microtubules decorated with 1.5-2 nM kinesin-1. Assuming a fractional occupancy of 50% for a kinesin-1 concentration that equals the dissociation constant $K_{d,MT}$ (Fig. 8) only every 10^{th} binding site of 'template' microtubules loaded in solution was occupied.

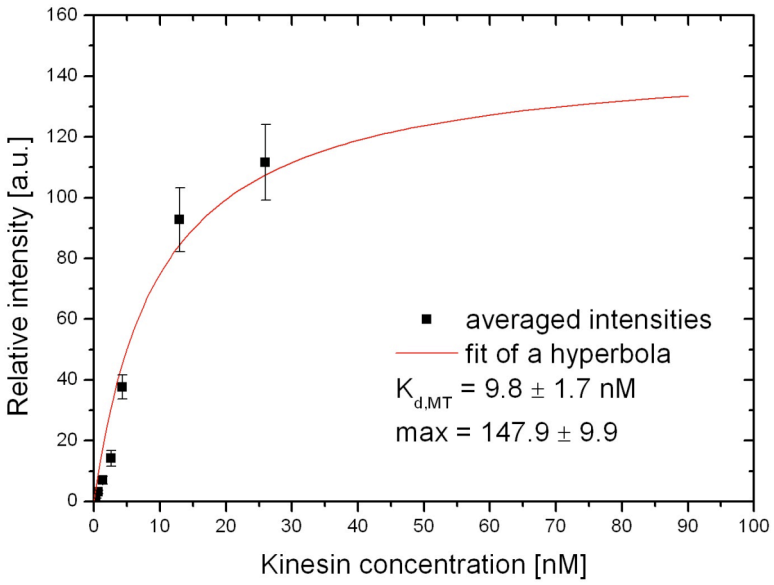

Figure 8: Fluorescent intensity of surface-immobilized microtubules loaded with GFP-labeled kinesin-1 inside the flow-cell. The intensity data (±standard deviation) was plotted in dependence of the kinesin-1 (dimer) concentration, and was fit to a hyperbola according to the law of mass action. Each data point thereby represents the average intensity of 25 microtubules. $K_{d,MT}$ was determined to be 9.8 ± 1.7 nM.

An example of the final generation and usage of a stamped kinesin-1 'nanotrack' is shown in Figure 9. Transport microtubules frequently bound to the stamped kinesin-1 molecules and moved either precisely along or under some angle across the tracks. Sometimes, a microtubule walking across a track changed its direction, aligned with the track and moved further along the track.

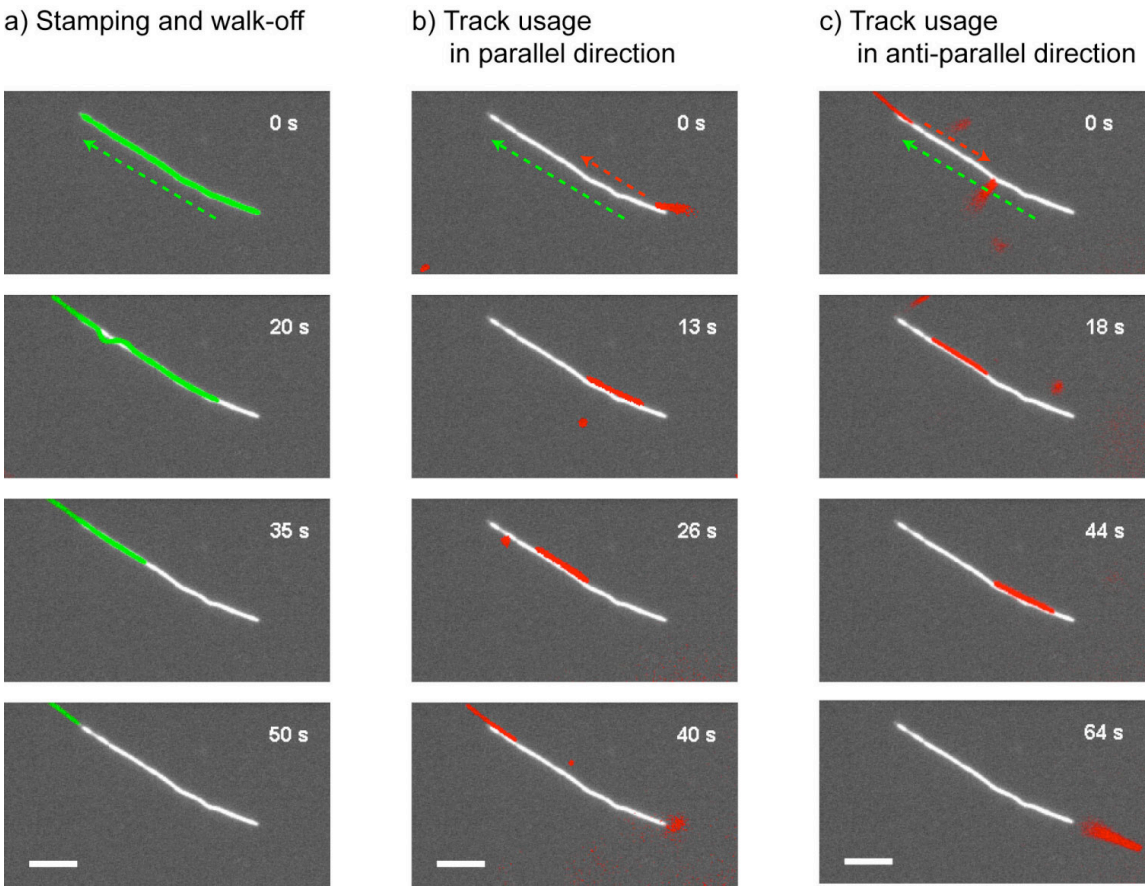

Figure 9: Generation and usage of stamped kinesin-1 nanotracks. The location of the tracks was inferred from fluorescent micrographs of the kinesin-1-decorated template microtubules before ATP addition (shown in white). Real-time images of moving template and transport microtubules are superimposed in red and green, respectively. **a**, Track generation. Immediately after ATP addition the template microtubule (green) started to move one filament length, detached from the surface and left a track of kinesin-1 molecules on the surface. **b**, A transport microtubule (red) followed the created track in the direction the template microtubule had walked off. **c**, Another transport microtubule (red) followed the same track opposite to the walk-off direction and detached from the track after reaching its end. Scale bars represent 5 µm. Arrows indicate the directions of movement.

Analysis of the movement showed that microtubules preferably walked well-guided along the tracks (Fig. 10a). Movement thereby occurred with equal likelihood in the direction in which the template microtubule had walked off the track or in the opposite direction. This behavior is expected because (i) the high torsional flexibility of the kinesin-1 molecules [156] allows the kinesin-1 heads to bind microtubules in any orientation, and (ii) the two-fold symmetry of dimeric kinesin-1 molecules [34] supports binding in either direction. Thus only the orientation of a transport

microtubule determines its direction of movement. Transport microtubules moved with similar speeds along the tracks in either direction. This speed was, moreover, independent of filament length and equaled the speed observed during walk-off (Table 1).

Walk-off (μm/s)	Track usage (both directions) (μm/s)	Track usage parallel to walk-off (μm/s)	Track usage anti-parallel to walk-off (μm/s)
0.62 ± 0.11 (n = 39)	0.59 ± 0.16 (n = 39)	0.56 ± 0.14 (n = 22)	0.63 ± 0.17 (n = 17)

n = number of evaluated microtubules

Table 1. Mean gliding velocities (mean ± standard deviation) of microtubules along stamped kinesin-1 nanotracks.

Once moving along a kinesin-1 track the guiding probability was larger than 80 % (n=60 microtubules), meaning that 80% of the transported microtubules followed the tracks to their ends. The reasons for not being guided were either a low kinesin-1 density on the track, which was in some cases insufficient for very short microtubules (< 2 μm), or kinks in the tracks that microtubules could not follow. Taking into consideration the lengths of the smallest microtubules that reliably moved along the tracks the motor density was estimated to be at least 0.7 functional kinesin-1 molecules per μm.

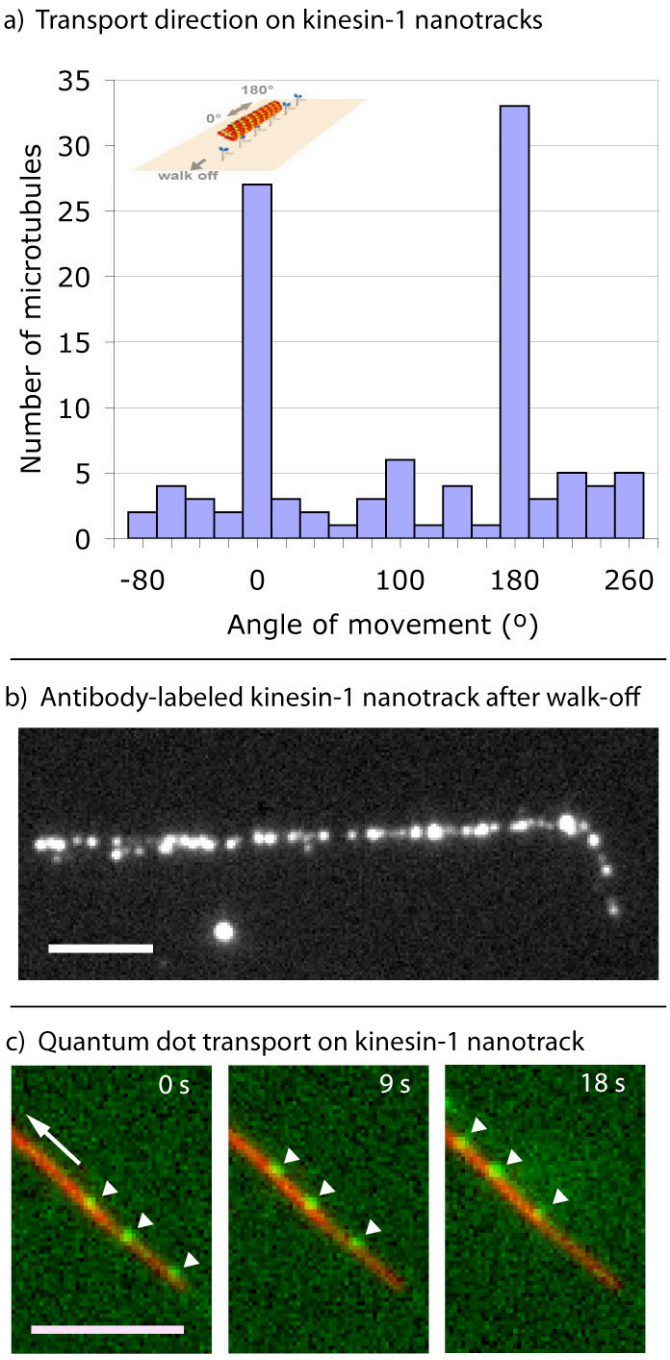

Figure 10: Evaluation and application of stamped kinesin-1 nanotracks. **a,** Distribution of movement directions on the stamped kinesin-1 tracks with respect to the walk-off direction of the template microtubule. While movement along the tracks (0 and 180°) was predominant, movement across the tracks occurred at statistically distributed angles. **b,** Fluorescent image of a kinesin-1 track labeled with anti-kinesin and a FITC-labeled secondary antibodies after the template microtubule had walked off. **c,** Cargo transport along a kinesin-1 nanotrack. Real-time images of three quantum dots (shown in green) that were bound to a motile transport microtubule (not shown) are superimposed to a fluorescent micrograph of the template microtubule before walk-off (shown in red). Scale bars represent 5 µm.

To further characterize the motor tracks the stamped kinesin-1 molecules were labeled with anti-kinesin antibodies that specifically targeted an epitope at the motor domain (carboxyl terminus of the kinesin-1). Fluorescein-5-isothiocyanate (FITC) labeled secondary antibodies were then used to visualize the kinesin-1 locations on the surface (Fig. 10b). Although presumably not all kinesin-1 molecules were labeled by an antibody, the motors in the track appeared dense and homogeneously distributed. Because the anti-kinesin antibodies bound specifically to the motor domains, the labeling provided further evidence for the orientation of the kinesin molecules: the motor domains pointed away from the surface and were not attached to the substrate. This is of great importance for their biological activity and cannot be controlled by other direct protein patterning techniques, such as microcontact printing or dip-pen nanolithography.

Because kinesin-1 molecules decorate the whole surface of the template microtubules (not shown in Figure 7a) one can ask, whether the nanotracks will be significantly broadened by the random substrate binding of those kinesin-1 molecules released during walk-off. By evaluating fluorescence data, as presented in Figure 10b, it was found that only few motors bound to the surface unassociated with the tracks and their density was too low to support motility. The labeling technique using the fluorescent antibodies also allowed us to quantitatively estimate the lateral width of the stamped tracks. Fitting the fluorescence intensity profile perpendicular to the track in Figure 10b by a Gaussian function proportional to $e^{-r^2/2w^2}$ (averaged over a microtubule length of 4 μm) yielded an apparent width of w_{AB} = 382 ± 6 nm. Due to the limited optical resolution, this value represents the convolution of the real track width w_{track} with the one-dimensional point-spread-function (width w_{PSF}) of the imaging system. If a Gaussian-like distribution for the locations of the track-forming kinesin-1 molecules is assumed the track width can be estimated by

$$w_{track} = \sqrt{w_{AB}^2 - w_{PSF}^2}, \qquad \text{(Equation 2)}$$

which represents the deconvolution of two Gaussian functions [157]. Because the lateral width of a microtubule is at least 10 times smaller than the optical resolution of the imaging system, it is reasonable to approximate w_{PSF} by measuring the fluorescence intensity profile perpendicular to a fluorescein labeled reference microtubule. Such a measurement yielded 328 ± 8 nm and the actual lateral width of the kinesin-1 track was thus determined to be w_{track} = 195 ± 18 nm. Although being a

rough estimate, this value documents the narrow width of the track. On the other hand, it exceeds the width of the template microtubule by multiple times. Physical reasons for this broadness were presumably: (i) a non-perfect straightness of the template microtubule along the length over which the intensity profile was averaged, (ii) kinesin-1 molecules (contour length of about 70 nm) that were bound on the sides of the template microtubule, and (iii) some broadening of the apparent track width due to the antibody labeling procedure. Moreover, because the localization accuracy of fluorescent objects is limited by the number of detected photons [158] the determined track width has to be considered as an upper limit.

Toward the usability of the stamped kinesin-1 tracks for nanotechnological applications an additional experiment was performed. Streptavidin-coated quantum dots bound to biotinylated transport microtubules were transported as model nanocargo along the tracks (Fig. 10c).

Moreover, it was observed that sometimes the tracks were used by multiple microtubules (with and without cargo) at the same time, occasionally even with microtubules passing each other in opposite direction (data not shown).

The experiments on motor stamping confirm earlier studies, in which motor proteins were deposited using filaments themselves to infer biophysical data on the flexibility of myosin heads [159] and on the behavior of oriented dynein arrays [160]. Here, this approach was advanced to kinesin-1 motors and demonstrated the suitability of such motor tracks for the setup of guided nano-transport systems.

3.2 Biotemplated binding of kinesin-1 and kinesin-14

Biotemplated binding of motor proteins (see again Figure 7b (on page 20)) was demonstrated using kinesin-1 and ncd motors. In a first approach, biotinylated kinesin-1 molecules were bound via streptavidin to biotinylated template microtubules that were immobilized on the surface using specific antibodies. Figure 11 shows examples of track usage by transport microtubules. To reduce the unspecific surface-binding of streptavidin and kinesin-1 it was crucial to block the glass surface with a polyethyleneglycol-terminated copolymer (Pluronic F127) after application of the antibodies. In experiments where the template microtubules were immobilized by anti-tubulin antibodies (Fig. 11a and b) free tubulin was added to the motility solution in order to saturate the microtubule binding sites of those antibodies and thus to avoid

static binding of transport microtubules to the surface. A further and almost complete reduction of the undesirable interactions of the transport microtubules with the surface became possible when the template microtubules were immobilized by anti-rhodamine antibodies and transport microtubules labeled with Alexa 488 were used. Using either immobilization procedure the transport microtubules followed the tracks precisely in either direction. In total 27 transport microtubules were imaged moving along biotinylated kinesin-1 tracks. In all guiding events, no microtubule was observed to be pushed off the tracks by the motors and neither did any microtubule move unspecifically on the surface. These results confirm that efficient chemical guiding along narrow kinesin-1 tracks is possible. Moreover, compared to biotemplated stamping the binding approach enables higher motor densities on the tracks since template microtubules are immobilized on the surface and cannot cluster.

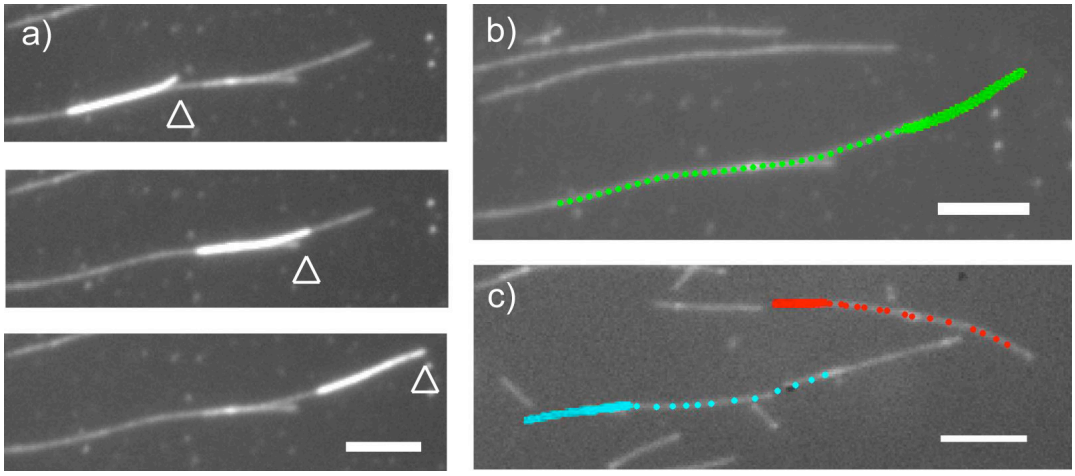

Figure 11: Usage of biotinylated kinesin-1 tracks on surface-immobilized template microtubules. a, Sequence of fluorescent images showing one transport microtubule (brightly labeled) moving on a template microtubule (dimly labeled) immobilized by anti-tubulin antibodies. Time between frames: 20 s. **b** and **c,** Overlays of template microtubules (white) immobilized by anti-tubulin antibodies (b) and anti-rhodamine antibodies (c) with the paths of transport microtubules (colored). The paths were determined by automated tracking of the ends of the motile transport microtubules. Scale bars represent 5 µm.

In a second approach, ncd motor molecules were bound to antibody-immobilized template microtubules via their second, ATP-independent microtubule binding site [161]. Because template microtubules were frequently ruptured off the surface by ncd motors that nonspecifically bound to the antibodies (control data with

GFP-labeled ncd not shown), template microtubules were additionally fixed to the surface using glutaraldehyde. This treatment, which preserves the microtubule structure [73, 162], was found to also reduce nonspecific binding of ncd to the surface. To remove free motor from solution and ensure that only bound motors remained in the flow-cell, the sample was extensively rinsed with buffer. Figure 12 shows examples of track usage by transport microtubules. Less than 10% of the microtubules (n=80) moved across the tracks at arbitrary angles - some even becoming aligned with the tracks during their movement. Presumably, this alignment behavior, which was superior to the guiding achieved with kinesin-1 motors, originated from the fact that ncd is a non-processive motor. Each ncd molecule undergoes only one catalytic cycle per encounter with a microtubule and about 4 ncd molecules are required to work in concert to continuously move a microtubule [64]. Therefore non-aligned movement of a transport microtubule across a ncd-track, where the number of motors is strongly limited, is rather unlikely. Non-processive microtubule motors might thus provide an advantage over processive ones in terms of reliable guiding and transport on the nanoscale. The shortest moving microtubules that were propelled continuously along the ncd tracks had a length of 0.8 μm. Based on the fact that 4 motor molecules are necessary for continuous gliding [64] the motor density on the tracks was at least 5 functional ncd molecules per μm.

Notably, moving microtubules were often tethered to the track with their trailing minus ends whereas the leading plus ends frequently lifted up. This might have been the result of a prolonged residence time of ncd molecules at the microtubule minus ends, which were in fact observed in experiments using GFP-labeled ncd (data not shown). In terms of redirecting the movement of transport microtubules at track crossings and branching points, this behavior was found to be advantageous and reorientation onto the track geometry was even possible at T-like junctions (Fig. 12b). Moreover, it was observed that microtubules walked in both directions along the tracks and were able to pass each other while sliding on the same track (Fig. 12c). Due to the torsional flexibility in the ncd molecules exclusively immobilized on the template microtubules, such bidirectional track usage was expected.

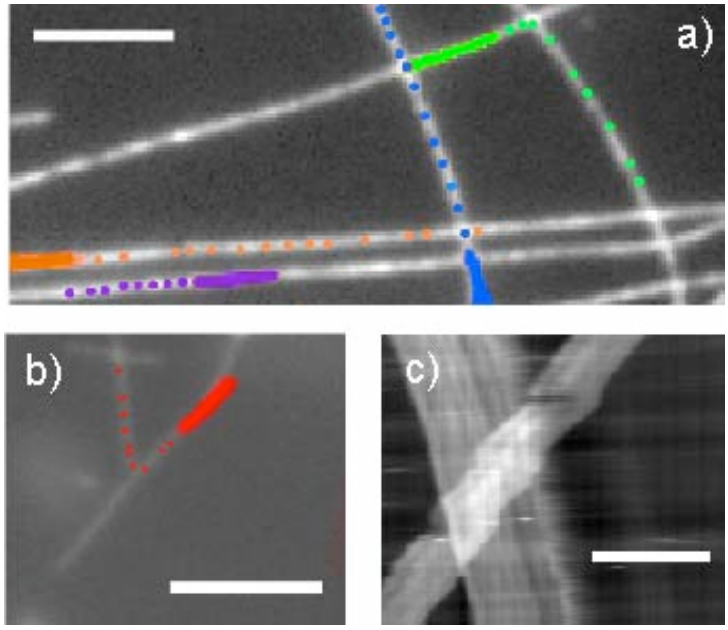

Figure 12: Usage of Ncd tracks on surface-immobilized template microtubules. a, Overlay of template microtubules (white) immobilized and fixed by glutaraldehyde with the paths of transport microtubules (colored). The paths were determined by automated tracking of the ends of the motile transport microtubules. **b,** A microtubule took a turn at a track crossing and got redirected. **c,** Kymograph (horizontal: fluorescence intensity profile along the template microtubule, vertical: time, 170 s) showing two transport microtubules that were sliding contemporaneously on one track in opposite directions. Scale bars represent 5 µm.

3.3 Biophysical application: Directional sliding of kinesin-14

The arrangement of microtubule-microtubule sliding by ncd, as demonstrated in the previous chapter, closely corresponds to the arrangement of microtubules in the mitotic spindle. The mitotic spindle is a molecular machine composed of a bipolar array of microtubules whose minus ends are focused at the spindle poles and whose plus ends confine a midzone of overlapping microtubules with opposite polarity (Fig. 13). This complex organization is achieved by the activity of molecular motors that generate forces towards the minus and plus ends of microtubules [163-165]. In particular, ncd has been proposed to participate in spindle organization by establishing contacts between adjacent microtubules in the spindle midzone and near the spindle poles. However, the molecular mechanisms of ncd acting in-between microtubules is not known.

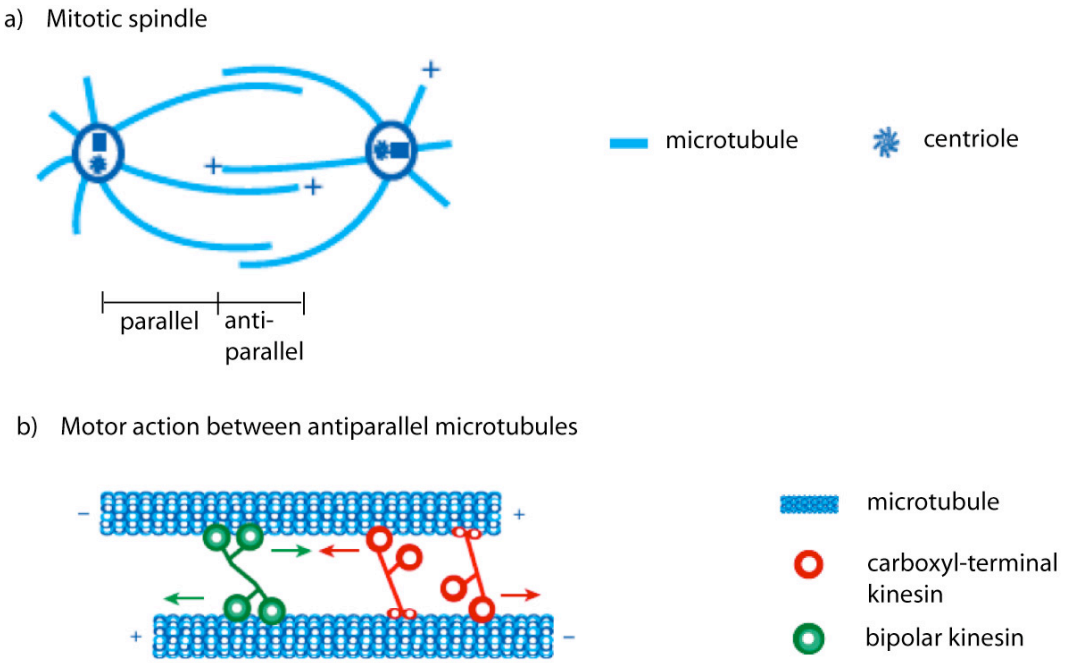

Figure 13: Microtubules and motors in the mitotic spindle. a, Schematic of the mitotic spindle. Bipolar array of microtubules emanating from the duplicated centrosomes with their plus ends. In the spindle midzone microtubules overlap with opposite polarity. **b,** Multiple molecular motors are generating forces in the spindle midzone between antiparallel microtubules. Figure adapted from [163].

While endeavors to apply biomolecular motors as nanomachines benefited a lot from advances in understanding how these motors work, the developed bionanotechnological approaches can, contrariwise, also substantially contribute to the understanding of motor function *in vivo*. Here, the biotemplated binding assay described before was applied again to specifically address ncd induced microtubule-microtubule sliding with respect to the microtubule polarities.

First of all, kymographs of GPF-labeled ncd molecules bound to the glutaraldehyde template microtubules with their ATP-independent microtubule binding site (Fig. 14) did indeed show extended periods of stationary binding. Such a configuration was assumed before as a prerequisite in order to generate ncd tracks for microtubule transport, and allowed bidirectional transport.

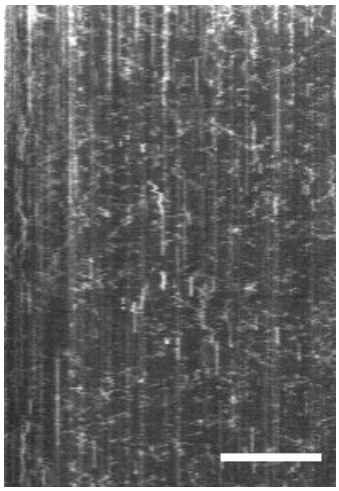

Figure 14: Ncd-interaction with microtubules in the presence of 1 mM ATP. GFP-labeled ncd molecules were imaged by total internal reflection (TIRF) microscopy with 10 frames per second. The kymograph (horizontal: fluorescence intensity profile along the immobilized microtubules, vertical: time, 30 s) shows predominantly stationary binding of ncd molecules on the immobilized microtubules. Thus, it can be assumed that ncd bound with its ATP-independent binding site to the microtubules. Scale bar represents 10 µm.

Secondly, the movement directions of transport microtubules were evaluated with respect to the polarity of the template microtubules. Thereby it was observed that microtubules were sliding with about equal probability in an antiparallel and a parallel configuration, respectively. However, when new ncd molecules were added into the flow-cell, transport microtubules sliding in parallel direction abruptly stopped while antiparallel ones remained sliding (Fig. 15). In fact, within one field of view 15 microtubules were sliding antiparallel and 14 microtubules were sliding parallel. But after adding extra motors 18 microtubules were observed sliding antiparallel whereas none of them was moving in a parallel arrangement (in the same field of view). This behavior can be explained in the following way: Part of the additional ncd motors presumably bound with their second, ATP-independent binding sites to the transport microtubules. The head domains of these motors could then interact with the template microtubule (see schematic diagram in Fig. 15c). In an anti-parallel arrangement the forces of all motors added constructively, leading to continued movement. In a parallel arrangement of template and transport microtubules these newly added motors then counteracted the movement of the ncd motors, which were immobilized on the template microtubules, resulting in an arrest of motility.

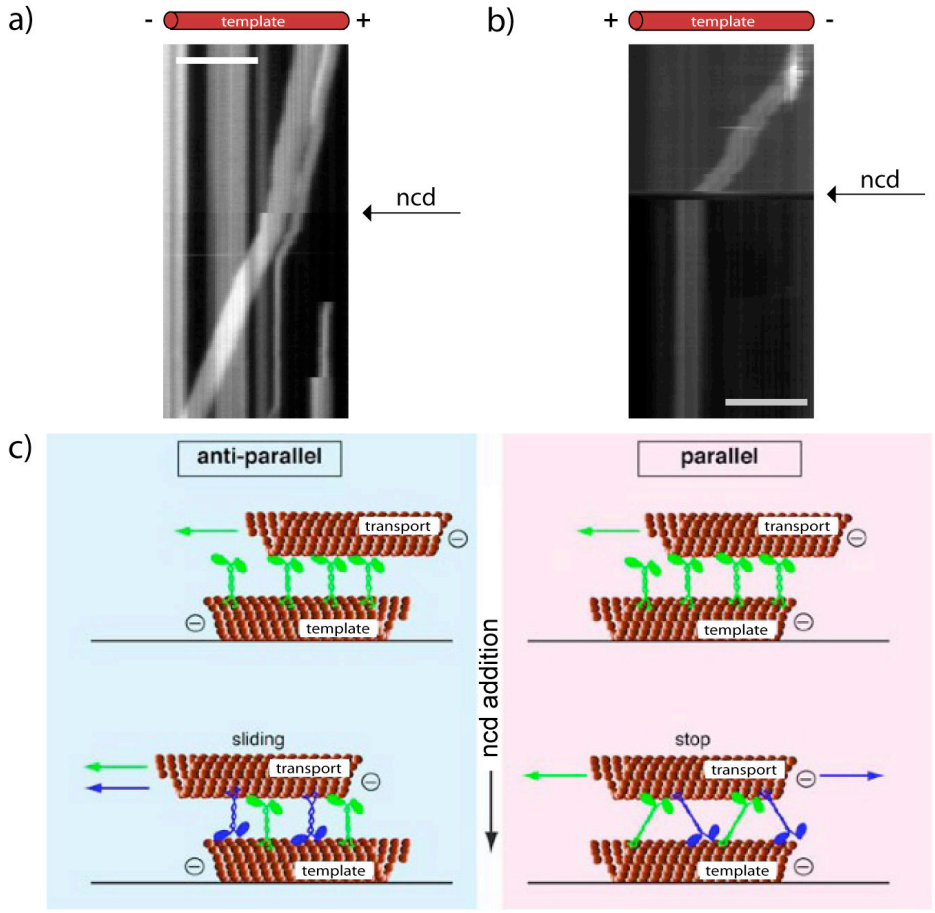

Figure 15: Directional microtubule-microtubule sliding and static cross-linking by ncd. **a,** Kymograph (horizontal: fluorescence intensity profile along the template microtubule, vertical: time, 350 s) of a brightly labeled transport microtubule sliding in antiparallel manner along a ncd track formed 'on top' of a polarity-marked template microtubule (polarity indicated above). This transport microtubule continues to slide along the track after the perfusion of additional ncd motors. **b,** Kymograph (horizontal: fluorescence intensity profile along the template microtubule, vertical: time, 500 s) of a brightly labeled transport microtubule sliding in parallel manner along a ncd track formed 'on top' of a dimly labeled template microtubules (polarity indicated above). This transport microtubule stops to slide along the track after the perfusion of additional ncd motors. **c,** Schematic diagram of the sliding behavior (adapted from [166]). For both, parallel and antiparallel microtubules, transport microtubules are propelled with their plus end leading by motors bound with their tail on the template microtubules. In anti-parallel sliding motors pull (blue motors) or push (green motors) the transport microtubules in the same direction. Thus their action is assisting. In parallel sliding the motors pull (blue motors) or push (green motors) the transport microtubules in opposite directions. Thus motors are counteracting and movement of transport microtubules is stopped. Colored arrows represent the forces onto the transport microtubules.

When these experiments were repeated in our laboratory under physiological conditions (other buffer; no glutaraldehyde treatment of microtubules) this behavior of directional microtubule-microtubule sliding could be confirmed [166]. However, it was found that the amount of stationary bound ncd molecules reduced to zero. The GFP-labeled motors rather diffused along the immobilized microtubules. Using different modified motor constructs it was shown that the diffusion was mediated by the tail. In microtubule-microtubule sliding assays ncd still diffused, but generated force with its head domain. Further, due to the loose binding, part of the motor molecules switched from the template to the transport microtubule. Thus a directional microtubule-microtubule sliding behavior was achieved even without the addition of extra motor molecules.

The experiments provided new insight into the actual mechanism by which ncd alone can induce directional microtubule-microtubule sliding (in the spindle midzone) and static cross-linking (near the spindle poles). Moreover, the observed dynamic interactions help to understand the assembly of complex microtubule arrangements [167], the modulation of spindle length, and spindle collapse [168, 169]. Thus, biotemplated patterning proved to be a promising tool for *in vitro* studies on the individual and cooperative behavior of various microtubule crosslinking proteins and motor proteins as well as for the reconstitution of complex subcellular machineries in synthetic environments.

4 Photothermal motor control on thermoresponsive polymer layers

The biotemplated patterning approaches described in chapter 3 proved that reliable guiding of microtubules on planar surfaces is possible. However, using microtubules as templates, it is not straightforward to create user-defined tracks. Additionally, the guiding performance of curved kinesin tracks cannot be systematically evaluated by the arbitrary track geometries resulting from the biotemplated stamping approach. Therefore, a new method for the freely programmed high-resolution patterning of biofunctional proteins was explored theoretically and experimentally.

The general idea of the patterning technique is based on localized light-to-heat conversion (LHC) combined with a surface-grafted thermoresponsive polymer layer. Previously it was demonstrated that poly(N-isopropylacrylamide) (PNIPAM) could be used to control the binding of proteins onto thermoresponsive surfaces [152]. There, the conformation of PNIPAM molecules in aqueous solution was switched in a spatially unstructured manner between the collapsed state at $T > 33°C$ (protein-binding conformation) and the swollen state at $T < 30°C$ (protein-repelling conformation). Here, this approach was extended by using optical signals of non-destructive visible light to generate heat in a highly-localized manner. In order to efficiently convert light into heat, a light-absorbing layer on the substrate was employed. Light radiation can interact with atomic systems through changes in the potential energy between atoms associated with the electronic excitation as analysis of the fundamental mechanism of light-to-heat conversion showed [170].

Spatial control over motile microtubules was achieved either by locally activating motors that are homogeneously distributed on a surface or by arranging motors in patterns (Fig. 16). In both approaches the sample is kept at low temperature to allow the PNIPAM chains to shield protein-binding. The incidence of visible light onto the light-absorbing layer on the substrate evokes localized heating and results in the collapse of the thermoresponsive polymer chains. When locally activating motors (Fig. 16a), surface-bound kinesin-1 molecules become accessible for microtubule binding and motility. When patterning motors (Fig. 16b), kinesin-1 molecules adsorb irreversibly on the substrate between the polymer chains. After illumination is turned

off the patterned proteins remain entrapped in the polymer layer. The produced pattern can then be reversibly activated and deactivated at elevated and room temperature, respectively.

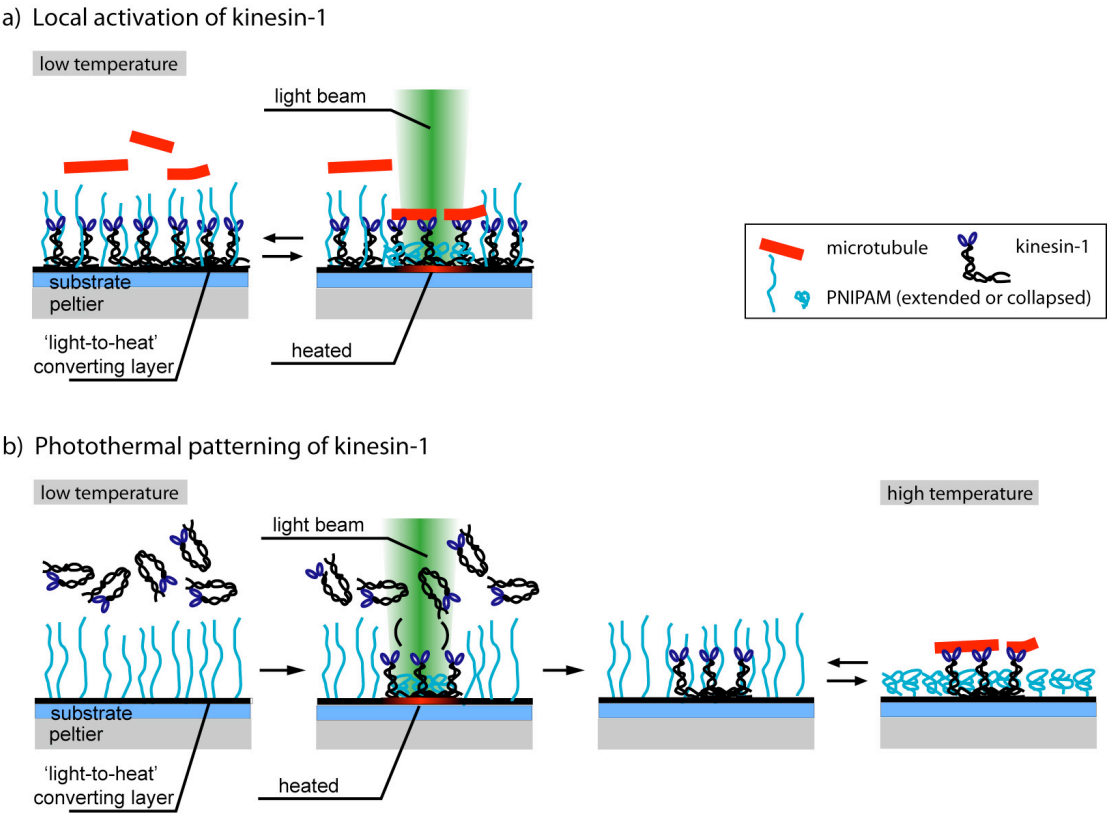

Figure 16: Photothermal motor control on light-to-heat converting surfaces with immobilized thermoresponsive polymer chains. a, Local activation of kinesin-1 molecules. Localized illumination and subsequent conversion of light into heat causes the collapse of the thermoresponsive polymer. In the illuminated areas, the surface-bound kinesin-1 molecules are activated and become accessible for microtubule binding. **b,** Photothermal patterning of kinesin-1 molecules. Localized heating upon illumination causes the collapse of the thermoresponsive polymer, resulting in adsorption of proteins in the illuminated areas. When the illumination is removed, the photopatterned proteins remain entrapped in the polymer layer, and the swollen polymer chains prevent further protein binding. At high temperature the patterned kinesin-1 molecules become accessible for microtubule binding.

4.1 Local heating and activation of kinesin-1

To experimentally confirm that the conformation of PNIPAM grafted to a LHC-layer was indeed switched due to light-to-heat conversion the following approach was used: A regular kinesin-1 gliding motility assay was performed at 35°C. After adjusting the temperature to 20°C microtubules were released from the surface, demonstrating the functionality of the PNIPAM. The surface was then illuminated continuously through a circular aperture opening with green laser light while keeping the backside of the substrate surface at 20°C by the means of a peltier element. Microtubules started to land and glide exclusively in the illuminated area within less than one minute of illumination (Fig. 17). Control experiments on similar surfaces, but without the LHC-layer, did not show microtubule binding upon illumination (data not shown). Thus, this experiment provided reasonable evidence for light-induced heating of a LHC surface. Moreover, it showed that kinesin-1 can be locally activated by light quite easily on a surface homogeneously covered with kinesin-1 molecules (as displayed in Figure 16a).

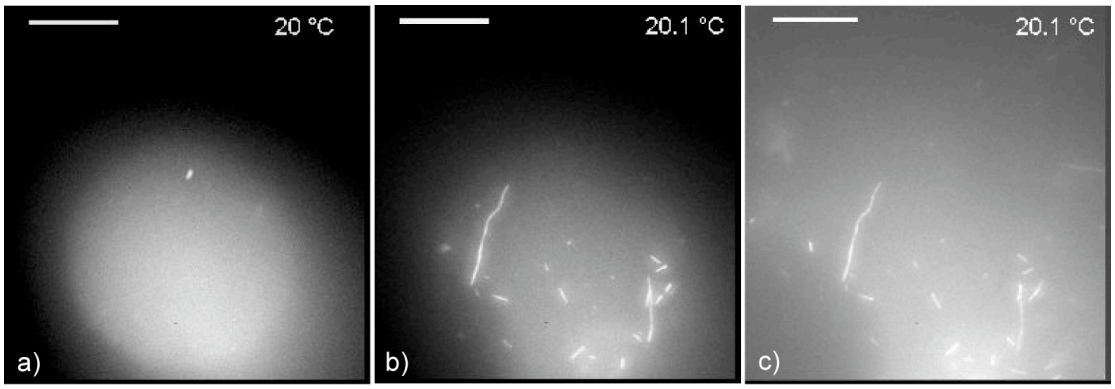

Figure 17: Local activation of kinesin-1 by light-induced heating of a PNIPAM coated surface. a, When keeping the sample at 20°C microtubules were prevented from binding to the surface-bound kinesin-1 molecules because the PNIPAM chains are swollen (see area of the aperture opening). **b,** Upon continuously illuminating the surface locally with green laser light, the surface locally heated up, and microtubules bound within the illuminated opening of the aperture. **c,** Opening the aperture proved that microtubules only bound in the illuminated area and not in the surface parts around. Scale bars represent 25 µm.

As the gliding velocity of microtubules on kinesin-1-coated surfaces is known to strongly depend on temperature [171-173], time-lapse fluorescence microscopy of

moving microtubules was used to estimate the temperature of the surface when illuminated. In order to calibrate the gliding velocity with respect to the temperature, a gliding motility assay was performed on a surface with PNIPAM as well as on a control surface without PNIPAM. Because of their high thermal conductivity, silicon substrates were used for assuring that the surface temperature equaled the temperature set by the peltier element. The temperature was varied within the range of 5°C to 46°C. Microtubules were still able to glide at 46°C. There was, however, an enhanced tendency of microtubules to detach from the surface due to the thermal denaturation of kinesin-1 molecules. On that account, data was evaluated only for temperatures up to 42°C. On PNIPAM surfaces microtubules were able to bind to surface-bound kinesin-1 and to glide over the surface at 28°C. This value is slightly below the LCST of PNIPAM but could be explained by the ability of microtubules to access the motor heads of the surface-attached kinesin-1 molecules at temperatures at which the polymer chains are not fully collapsed. For each data point velocities of at least 45 microtubules were determined. The data (mean velocity ± standard deviation) are illustrated in Figure 18.

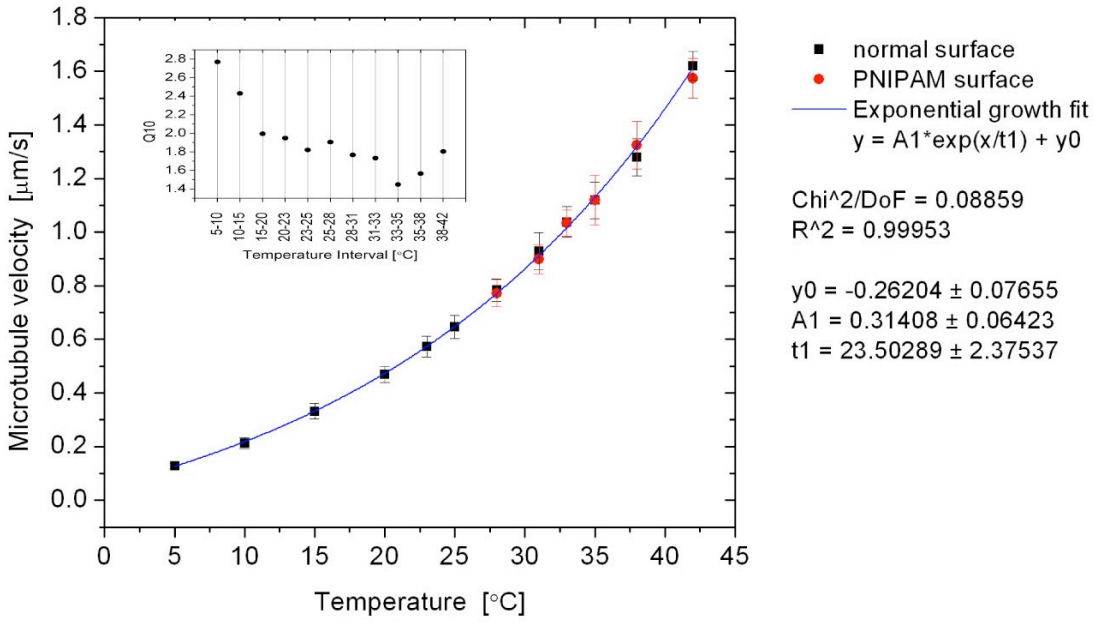

Figure 18: Dependence of microtubule gliding velocity on temperature. The velocities were fitted with an exponential growth function $y = Ae^{x/t} + y_o$. The inset displays the calculated Q_{10} values for the respective temperature intervals.

The temperature coefficient Q_{10} represents the factor by which the microtubule velocity v increases for every 10-degree rise in the temperature T and was calculated according to the following equation

$$Q_{10} = \left(\frac{v_2}{v_1}\right)^{\left(\frac{10}{T_2 - T_1}\right)}. \qquad \text{(Equation 3)}$$

In average Q_{10} was found to be about 2 (see inset in Figure 18), typical for chemical reactions. It was higher at lower temperatures and lower at higher temperatures. Further, the results are in good agreement with the data presented by Kawaguchi and Ishiwata [172], who examined the temperature effect on single kinesin-1 molecules using a bead assay. A break in the velocity increase at 27°C as was shown by Boehm et al. [173] in a gliding motility assay could however not be observed. Therefore, the α-helical conformational change of the amino-terminal coil of the kinesin-1 stalk that was observed at 25-30°C by means of circular dichroism spectroscopy [174], did not impact the velocity in our microtubule-gliding experiments.

The obtained temperature-velocity calibration curve was used to estimate the local heating effect evoked by the incidence of green laser light onto carbon layers on glass substrates with respect to the optical power. Thereby, it was mainly important to find conditions were the surface was heated above the LCST but at the same time to avoid overheating and denaturation of proteins. Thus, a gliding motility assay was performed on a carbon coated glass coverslip. The sample was kept on the peltier at 20°C and a collimated laser beam with parallel light locally illuminated the surface in a circular area through an aperture (Fig. 19a). The laser power was varied between 20 mW and 165 mW. During continuous illumination of the sample, time-lapse images were acquired for measuring the gliding velocity of microtubules. For each velocity a temperature was calculated by applying the temperature-velocity calibration curve. Both parameters, velocity and temperature, were plotted as a function of the laser power (Fig. 19b and c). The velocity curve showed an exponential increase whereas the temperature showed a linear one. This is reasonable because the temperature was calculated from the velocity values by a logarithmic equation. The linear dependence of the temperature on the laser power was later also supported by simulations as discussed in chapter 4.3.

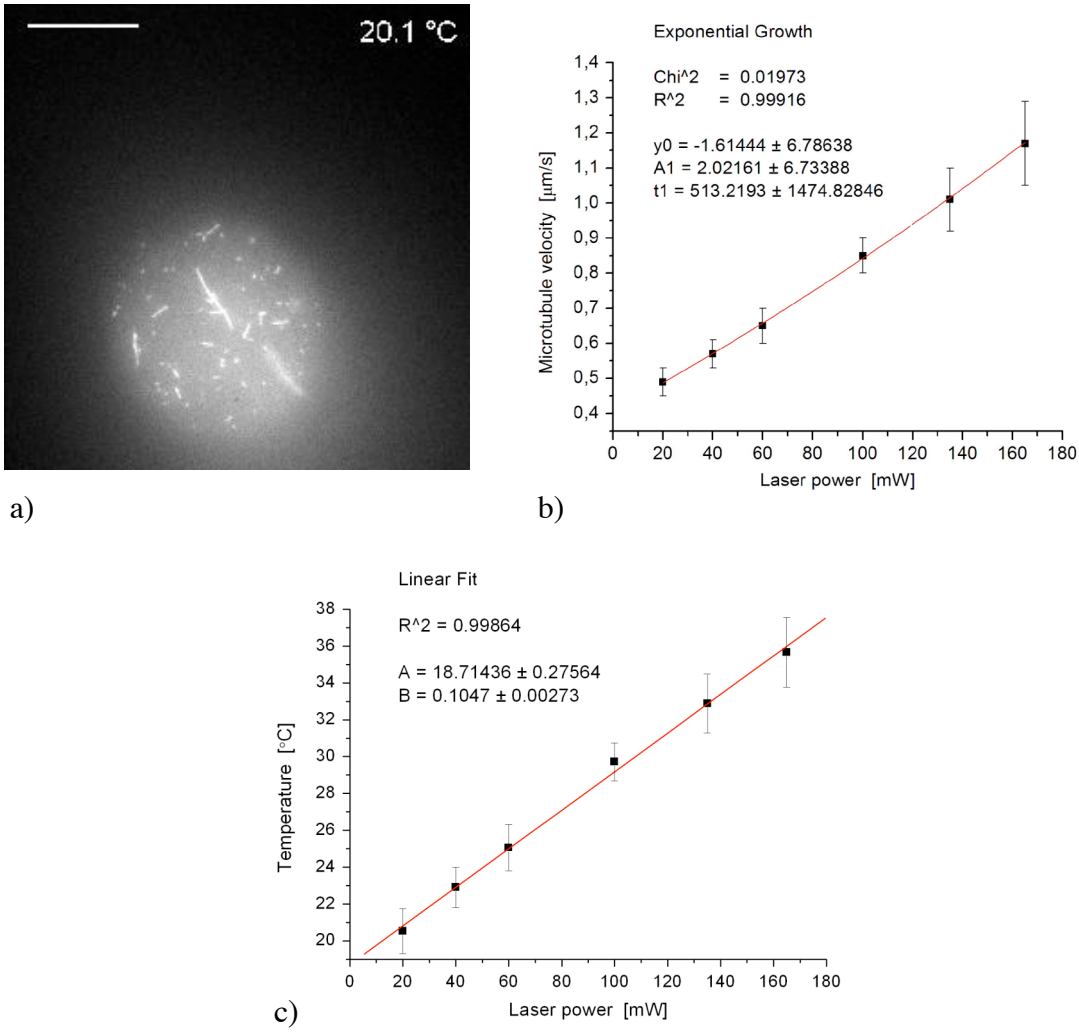

Figure 19: Dependence of local heating on optical power. a, Microtubules gliding on a carbon-coated surface within a circular area that was illuminated through an aperture. **b,** The velocity (± standard deviation) of at least 15 microtubules was measured for different optical power values. The data was best fitted with an exponential function ($y = Ae^{x/t} + y_o$). **c**, The temperatures, determined by applying the temperature-velocity calibration curve, showed a linear dependence ($y = A + B\,x$) on the laser power.

On PNIPAM-coated samples, kept at 20°C, binding of microtubules was observed for laser powers of 100 mW or greater, corresponding to temperatures of 29.5°C and above. This compared well to the microtubule binding temperature determined in the temperature calibration experiments (Fig. 18). At 135 mW, the laser power later used for kinesin-1 patterning, the temperature increase was about 12 K. However, this value was dependent on the exact size of the illuminated area.

4.2 Photothermal patterning of kinesin-1

Photothermal patterning of proteins (see again Figure 16 (on page 36)) was tested on the example of kinesin-1 molecules. Patterning experiments were performed by incubating kinesin-1-casein solutions onto PNIPAM-coated carbon-glass samples. The samples were kept at low temperature, e.g. 22°C, so that the PNIPAM was swollen and therefore protein-repelling. For illuminating the surface a collimated laser beam with parallel green light was employed. An aperture cut off part of this light so that only an area of the desired pattern size and shape was illuminated. The surface was illuminated for 2 min in order to allow the kinesin-1 molecules to bind out of solution. After turning off the illumination, unbound protein was washed out. Successful patterning and functionality of patterned proteins were then confirmed by microtubule-based gliding motility assays. For this, the temperature of the sample was raised to 35°C to collapse the PNIPAM chains on the entire surface and allow microtubules to bind to the patterned kinesin-1 molecules.

The experiments proved that kinesin-1 molecules could be patterned reproducibly onto PNIPAM-coated carbon-glass samples via photothermal patterning. Gliding microtubules in the formerly illuminated areas demonstrated that locally adsorbed proteins kept their biological function and were not denatured. In Figure 20 two examples are shown where the protein was adsorbed in a circular pattern. The patterned circles had diameters of about 30 µm, corresponding to the projected size of the aperture opening. The displayed traces of microtubules moving in the patterned area were determined by automated tracking. The circles in Figure 20e were patterned by sequential illumination steps. In-between each step the microscope stage was shifted 20 µm. Sequential patterning is important for specifically adsorbing different types of proteins next to each other. In another pattering experiment the aperture opening had the shape of a rectangle with 60 µm length and 20 µm height (Fig 20c). This proved the ability of the photothermal technique to create protein patterns with different geometries.

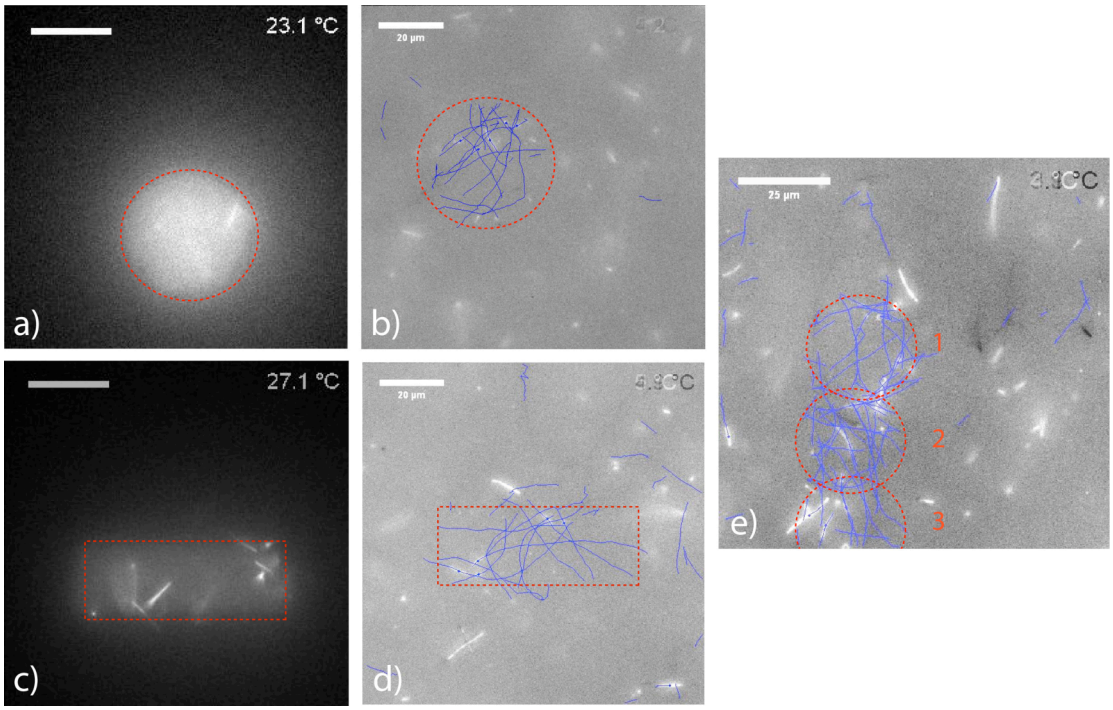

Figure 20: Results of photothermal kinesin-1 patterning. Kinesin-1 molecules were patterned by locally illuminating the sample through an aperture opening. The resulting patterns as well as the functionality of the molecules were visualized by moving microtubules. The traces of microtubules moving in the patterned circular area were determined by automatic tracking. The pattern positions within the field of view were slightly shifted with respect to the position of the aperture opening due to washing steps after patterning. The images (**a)** and **(c),** show a circular and a rectangular aperture opening, respectively. Scale bars represent 25 µm. In (**b)** and **(d)** the corresponding microtubule traces to (**a)** and (**c)** are displayed. Scale bars represent 20 µm. The image in (**e)** shows the microtubule traces in sequentially patterned circles. In this experiment the microscope stage was shifted 20 µm in-between each illumination step. Scale bar represents 25 µm.

Though microtubule binding and motility was mainly confined to the illuminated areas, few microtubules were also observed in non-illuminated surface parts. However, these microtubules were, in contrast to the ones moving in the patterned area, loosely bound to single motor molecules, often swiveled and mostly moved only short distances. The kinesin-1 molecules outside the patterns might be residual motors after washing out the patterning solution. These could bind anywhere to the surface upon increasing the temperature for motility. Other possibilities could be low protein binding despite the swollen PNIPAM chains or local defects in the PNIPAM layer. Nevertheless, because the edges of the patterns appeared relatively

distinct, it is rather unlikely that kinesin-1 molecules bound to the surface due to heating effects and PNIPAM collapse upon illumination. In such a case one would expect a gradual decrease of the motor density from the center of the pattern towards the outside, which was not observed in the experiments.

On a side-note: Microtubules tightly bound to the surface by several motors appeared in the fluorescent images on carbon layers dimmer than ones loosely bound by single motors and further away from the surface. This fluorescent intensity difference of the microtubules might be due to fluorescence interference contrast (FLIC) effects. FLIC occurs whenever fluorescent objects are in the vicinity of a reflecting surface. The resulting interference between the direct and the reflected light leads to a double $\sin^2$ modulation of the intensity of a fluorescent object as a function of distance above the reflecting surface [92, 175].

4.3 Finite element modeling of local heating

To investigate the potential of the photothermal patterning technique with respect to resolution, scalability, and applied materials the temperature distribution in the experimental system, which is evoked by the incidence of light onto the LHC-layer, was modeled. A schematic 2D representation of the experimental system is depicted in Figure 21 and was used for finite-element modeling.

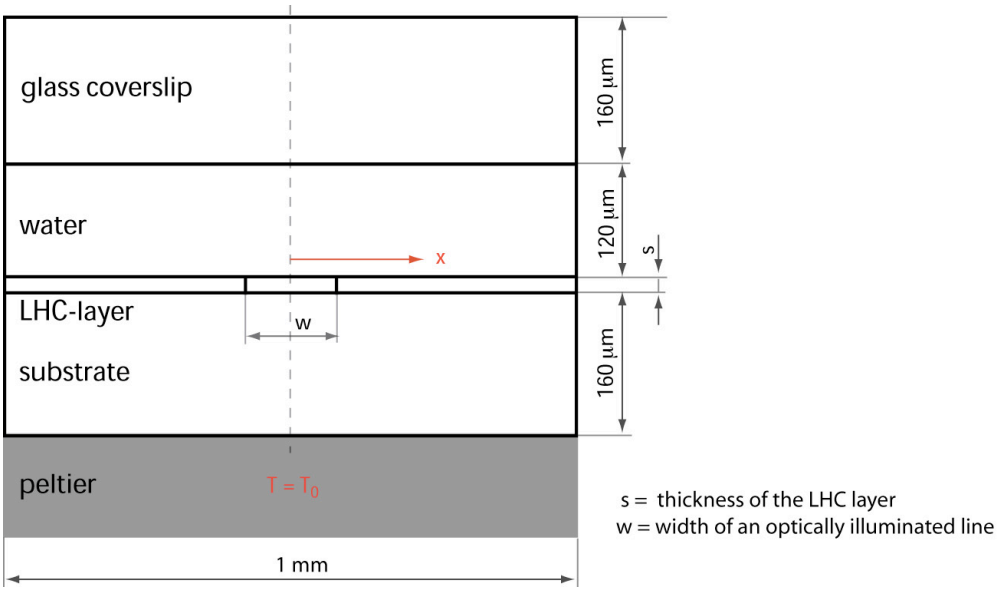

Figure 21: Schematic 2D model of the experimental system. The model consisted of five elements: the glass coverslip, the solution, the substrate, two non-illuminated parts of the LHC layer with the cross-section of the illuminated stripe in-between. Due to symmetry of the system the heat distribution along the surface of the LHC layer was only calculated for one side of the model. The parameter *x* was the distance from the center of the illuminated area. The bottom temperature was set by the peltier element and the temperature of the surrounding determined the constraint on the top. Figure not drawn to scale.

The finite-element-method (FEM) is a numerical approach for approximately solving partial differential equations (PDE) with boundary conditions. It is often used for the modeling and solving of scientific and engineering problems based on PDEs. The area of interest is thereby divided into any finite number of elements with finite sizes. Then, basis functions are chosen within the elements. When these functions are substituted into the PDE one obtains, together with the initial, boundary and transition conditions, an equation system that is normally solved numerically. The solution of the equation system represents finally the numerical solution of the PDE. For modeling the heat distribution in the system described above the software COMSOL Multiphysics was applied. This software allows building models by defining the relevant physical quantities - such as material properties, constraints, sources, and fluxes – rather than by defining the underlying equations. Variables, expressions, or numbers are directly applied to solid domains, boundaries, edges, and points independent of the computational mesh. COMSOL Multiphysics then internally compiles a set of PDEs representing the entire model.

The mathematical model for heat transfer by conduction was the following version of the heat equation,

$$\delta_{ts}\rho C\frac{\partial T}{\partial t}-\nabla\cdot(k\nabla T)=Q \qquad \text{(Equation 4)}$$

where T is the temperature, ρ is the density, C is the heat capacity, k is the thermal conductivity, δ_{ts} is the time-scaling coefficient, and Q is the heat source. Q describes the heat generated within a certain volume.

As boundary condition for all left and right boundaries of the model thermal insulation was chosen. The equation of the insulation condition

$$\mathbf{n}\cdot(k\nabla T)=0, \qquad \text{(Equation 5)}$$

with n being the normal component of the heat flux vector at a boundary, specified where the domain was well insulated, or it reduced the model size by taking advantage of symmetry. The equation states that the gradient across the boundary must be zero. For this to be true, the temperature on one side of the boundary must be equal to the temperature on the other side.

For each of the boundaries on top (room temperature) and on the bottom (peltier temperature) of the model, respectively, a prescribed temperature

$$T=T_0 \qquad \text{(Equation 6)}$$

was chosen individually. Thereby, the finite element solution returns a solution in which the above condition is either true or minimally approximated.

For all interior boundaries the continuity condition

$$-\mathbf{n}_1\cdot(\mathbf{q}_1-\mathbf{q}_2)=0 \qquad \text{(Equation 7)}$$

was applied, with q being the heat flux vector q = - k∇T. The heat flux in the normal direction is continuous across the boundary in this case.

After drawing the model and defining all physical quantities the software generated a triangular mesh and computed the solution.

Heat generated by LHC: When solving the model, the illuminated area was defined as the heat source. In order to get an idea about the dimension of the heat per volume generated by local illumination and LHC in the experimental setup the applied physical parameters were estimated.

In the experiments the laser power was set to 130 mW. The power that eventually came out of the objective was measured with a power meter and yielded a value of 20 mW (coupling efficiency of 15%). The laser intensity (I) was then roughly

estimated by dividing the power by the area illuminated with the collimated laser beam. This area was approximated to be about 0.01 mm^2 by measuring the diameter of the illuminated circle (d = 110 μm^2) in a microscopic image. The latter was taken with the 63x objective also used for patterning experiments. Assuming a laser beam with ideally parallel light the laser intensity equaled 2 W/mm^2.

The absorption of 20 nm thick potential LHC-layers was measured as a function of wavelength (Fig. 22). Carbon layers were mainly used for modeling and experiments since it has a higher absorption and a lower reflectivity than silicon.

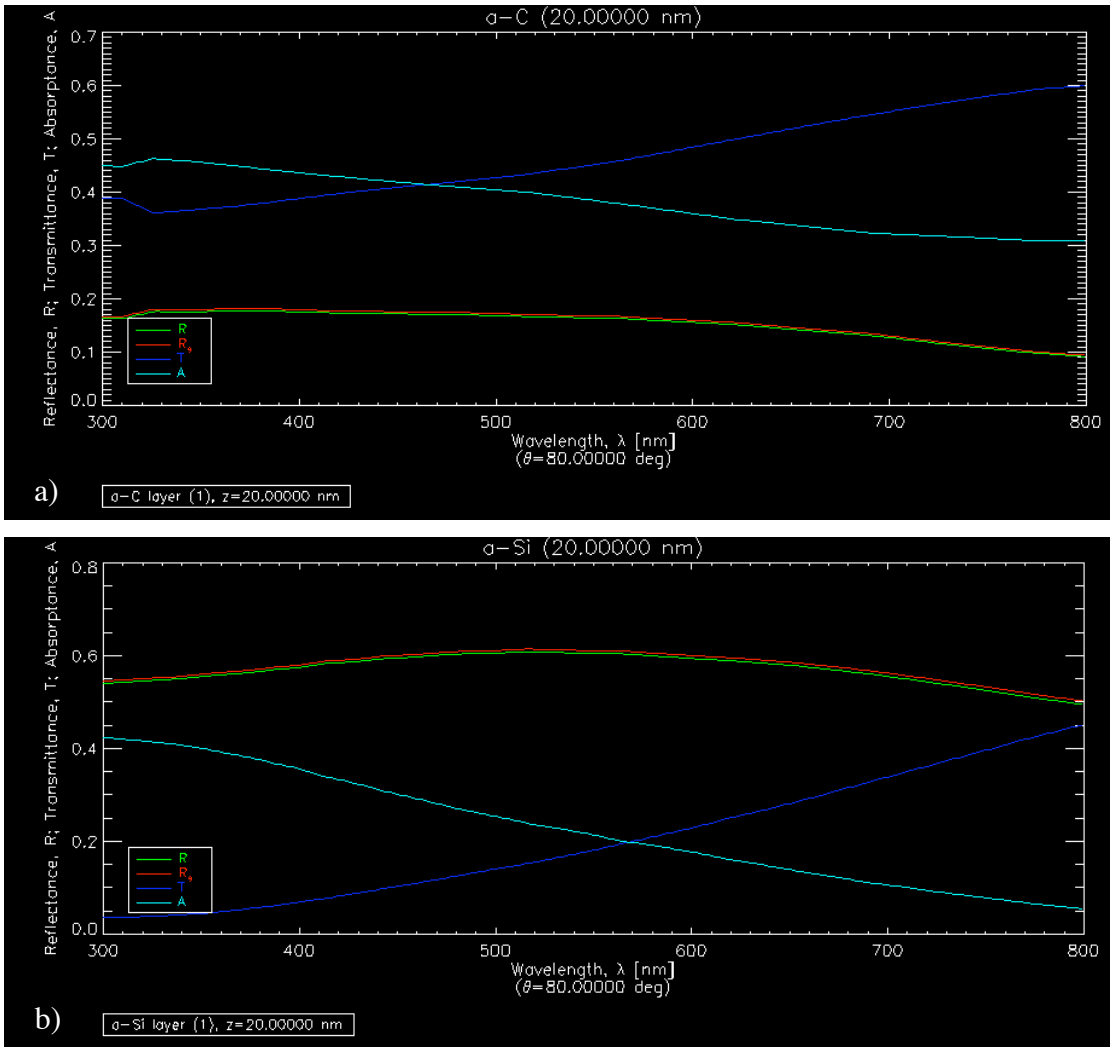

Figure 22: Optical properties of potential LHC layers. Reflectance (green and red), transmittance (dark blue) and absorption (light blue) are shown in dependency of the wavelength for **a,** 20 nm thin carbon and **b,** silicon layers. The spectra were determined with ellipsometry at the Fraunhofer IWS Dresden.

In order to determine the absorption in dependence of the distance the light travels through the material the Lambert-Beer law

$$T = \frac{I}{I_0} = e^{-y\alpha} \qquad \text{(Equation 8)}$$

was applied. T is the transmission, I_0 and I are the intensity of the incident light and that after the material, respectively, α is the absorption coefficient of the substance, and y is the path length / layer thickness. Using the measured transmission value for a certain wavelength, α was calculated. Transmission, absorption A, and reflectivity R were related as follows

$$A = 1 - T - R. \qquad \text{(Equation 9)}$$

From the calculated diagram of absorption / transmission versus layer thickness for carbon at a wavelength of 530 nm (Fig. 23) one can see that for a thickness of 100 nm an absorption of slightly more than 80 % is reached. However, carbon layers of 45 nm thickness already absorb about 70 % of the incident light.

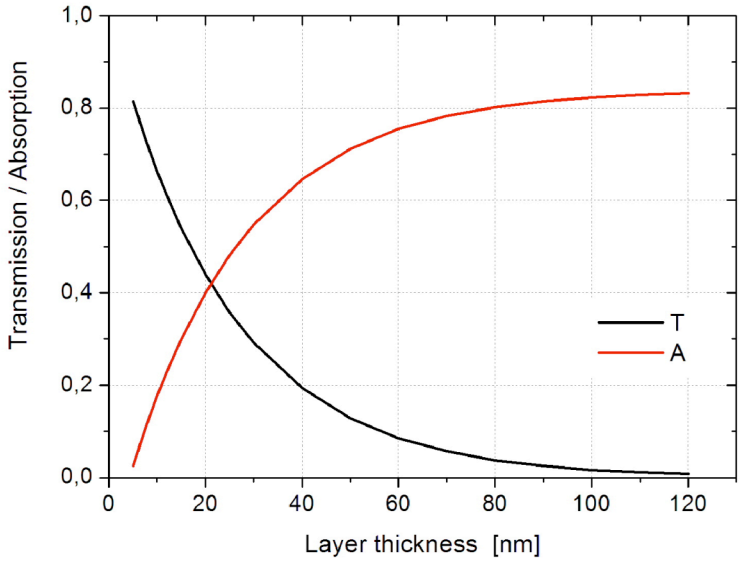

Figure 23: Transmission and adsorption of carbon in dependence of the layer thickness. The diagram was calculated for a wavelength of 530 nm.

According to the following equation,

$$Q = \frac{I\,A}{y}, \qquad \text{(Equation 10)}$$

the heat per volume Q resulting from the local illumination of a 45 nm thick carbon layer was finally estimated to be 3×10^{13} W/m^3.

Time-dependent temperature distribution: The experimental system was modeled in a time-dependent manner. Due to the symmetry of the model system the simulation of the temperature distribution was performed only for one half of it. In Figure 24a a typical 2D plot of the temperature distribution after 0.2 s of heating is shown. The solutions revealed that steady state conditions of heating and heat dissipation are reached in 100 ms (Fig. 24b).

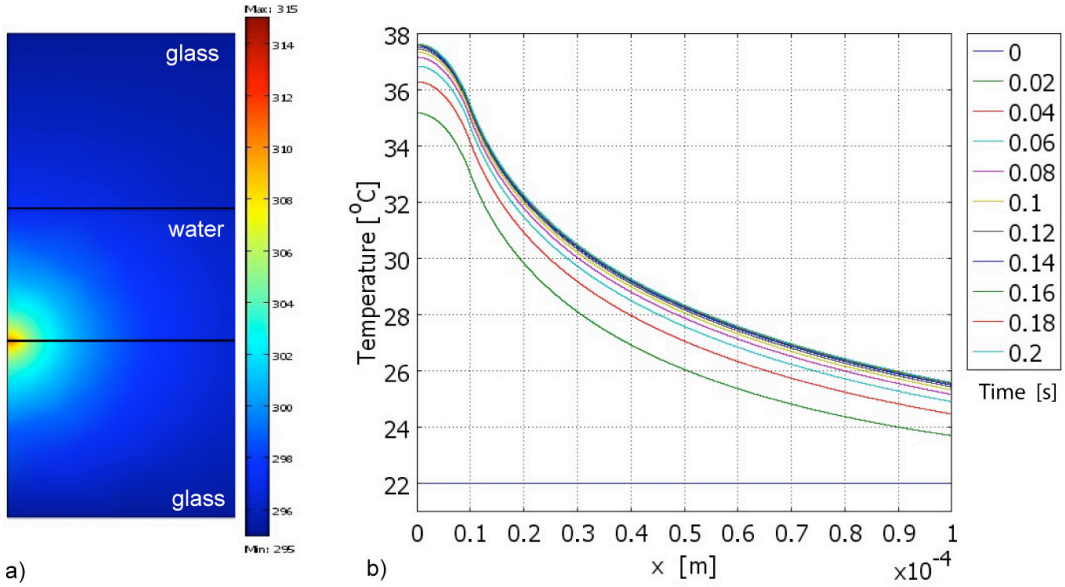

Figure 24: Time-dependent temperature distribution. The model system was a 45 nm thick carbon layer on glass**.** It was solved in a time-dependent manner for $Q = 3*10^{13}$ W/m^3 and $w/2 = 10$ μm. The temperature of the top and bottom boundary equaled 22°C. **a,** 2D temperature distribution in a section through the experimental system (as shown in Figure 21) after 0.2 s of heating for $x = 0$ μm to $x = 200$ μm. The temperature (unit: K) is color-coded. **b,** Time-dependant temperature distribution along the LHC surface. The solution of the temperature distribution was plotted for $t = 0$ s to $t = 0.2$ s every 0.02 s.

After the heat source is removed the system cools down similarly rapidly. Such time characteristic is desired because in this case the temperature response of the system is orders of magnitude faster than the kinetics of forming a protein monolayer (assuming typical diffusion coefficients (around 10^{-6} cm^2/s) and sticking probabilities for proteins). The surface adsorption process thus determines the illumination duration necessary for successful protein patterning.

With respect to the achievable resolution of the patterns using the photothermal patterning, the temperature distribution was simulated for (i) different Q values with

constant width of optical illumination, (ii) lower peltier temperature with constant illumination width, (iii) different illumination widths with constant Q, and (iv) different LHC materials with constant Q and illumination width.

Heat-dependent temperature distribution: In Figure 25 the temperature distributions along the LHC-surface, modeled for different Q values after 0.2 s of heating, are illustrated. First of all, the absolute temperatures in the simulations can be compared to the temperatures expected for experimentally creating 20 µm wide protein patterns on PNIPAM surfaces. Because the width of the generated kinesin-1 patterns were in the size of the illuminated area, showing distinct borders, the temperature at $x = w/2 = 10$ µm must have been about 32°C, the LCST of PNIPAM. Therefore, the simulated temperature profiles obtained for Q values between 2 and $2.5*10^{13}$ W/m^3 would better describe the experimentally expected temperature distribution than the estimated experimental value of $Q = 3*10^{13}$ W/m^3. However, though this value was only a rough approximation, the simulation results showed that the model fits the experiment quite well.

Secondly, as expected from the linear heat equation and the experimental results, the temperature values along the whole profile are linearly increased with increasing Q (see Table 2). This means that not only the maximal temperature is increased by higher Q values but also the temperature gradient between illuminated and surrounding areas becomes steeper. Further, it is easy to estimate the heat per volume necessary to achieve certain absolute temperatures for given illumination width and boundary temperatures.

$Q*10^{13}$ [W/m^3]	2	2.5	3	4
T_{max} [°C]	32.4	35.0	37.6	42.8
T_{max}-$T_{10\mu m}$ [K]	1.4	1.8	2.2	3.0
T_{max}-$T_{20\mu m}$ [K]	3.6	4.5	5.4	7.2

Table 2: Heat-dependent surface temperatures gained by solving the model system for w/2 = 10 μm according to Figure 25.

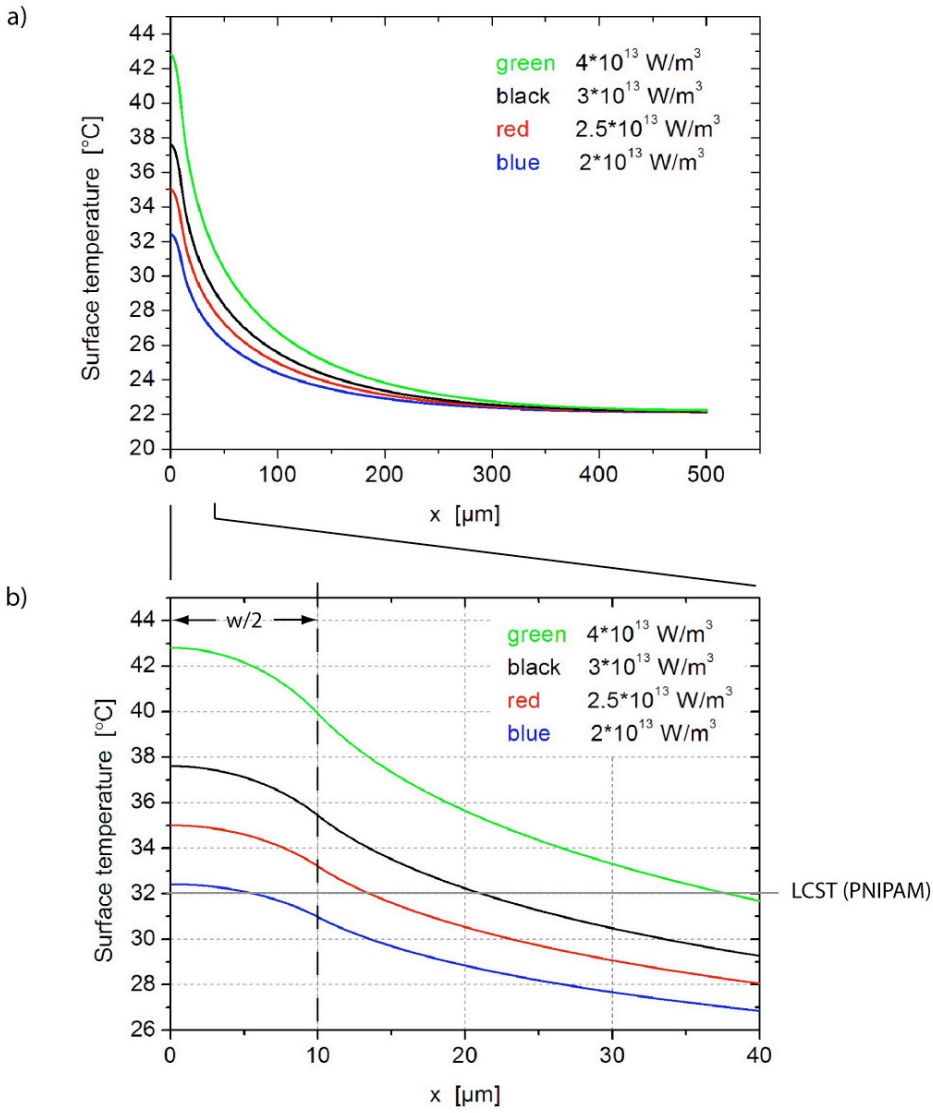

Figure 25: Heat-dependent temperature distribution along the LHC surface. The model system was a 45 nm thick carbon layer on glass with an illumination width of $w/2$ = 10 μm. **a,** Solution of the model for Q = 2; 2.5; 3; 4 *10^{13} W/m^3 after 0.2 s of heating. The temperature of the top and bottom boundary equaled 22°C. **b,** Temperature distribution in the illuminated area and the immediate surrounding (x = 0 – 40 μm, zoom into (a)).

Temperature distribution in dependence of the peltier temperature: The temperature distributions in dependence of the peltier temperature are shown in Figure 26. For constant Q values (Fig. 26a) the temperature curve is simply shifted by the temperature difference on the LHC surface. Here, one has to note that for glass substrates the LHC surface temperature (without illumination) does not equal the peltier temperature if the temperature of the surrounding is different. The reason is the low thermal conductivity of glass, which leads to an influence of the room

temperature on the temperature distribution. In the calculated example the temperature of the LHC surface was 17°C for a peltier temperature of 15°C and a surrounding temperature of 22°C. Therefore, the whole curve was shifted by 5 K (different from the 7 K difference in the peltier temperature).

While the maximal temperature does not change significantly when lowering the peltier temperature and simultaneously increasing Q, the temperature gradient becomes steeper (Fig. 26b). Though this is principally straightforward from the heat- and temperature-dependent simulation results described above it is interesting with respect to obtaining steep gradients without increasing the maximal temperature. A steep gradient is important to achieve a defined pattern size, ideally close to the width of the illuminated area. How steep the temperature gradient needs to be for sharp patterns, does however also depend on the switching characteristics of PNIPAM and the protein binding dynamics. These parameters could vary for different buffer conditions and types of proteins. In the literature it was reported that the extent of protein adsorption and its temperature-dependence varied with the molecular characteristics of proteins [176] (hydrophobicity, flexibility, and molecular size) as well as with the pH and the ionic strength of the buffer [177]. Given that the experimentally created kinesin-1 patterns where about the size of the illuminated area, as already mentioned above, the switching of kinesin-1 adsorption should be rather steep around the LCST. Assuming a stepwise switching from zero to maximal protein adsorption at the LCST it would even be possible to find conditions where the size of the patterned area is smaller than the illuminated area. An example of this case is the red temperature curve in Figure 26a, which crosses T = 32 °C (LCST) within the illuminated area of $x = w/2 = 10$ µm.

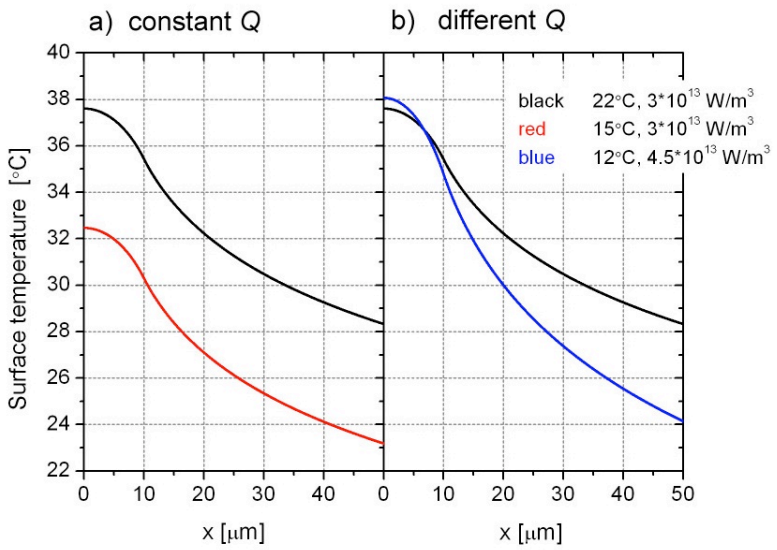

Figure 26: Temperature distribution along the LHC surface in dependence of the peltier temperature. The model system was a 45 nm thick carbon layer on glass with an illumination width of $w/2$ = 10 μm. The temperature distribution after 0.2 s of heating was simulated **a,** for T_{bottom} = 15°C and Q = 3*10^{13} W/m^3 (red curve) and **b,** for T_{bottom} = 12°C and Q = 4.5*10^{13} W/m^3 (blue curve). The temperature distribution T_{bottom} = 22°C and Q = 3*10^{13} W/m^3 (black curve) is displayed as comparison. The temperature of the top boundary equaled in all cases 22°C.

Temperature distribution in dependence of illumination width: When simulating the temperature distribution for different illumination widths (i.e. different aperture widths of the aperture opening) and constant Q values (Fig. 27) it became obvious that the optical intensity has to be increased significantly for realizing smaller patterns. This also means that there is a different optimal value of Q for each pattern size. Thus, experimentally, patterns of different dimensions cannot be achieved simultaneously e.g. by illuminating a surface through a mask with different stripe widths. One would either have to use laser scanning techniques or illuminate sequentially with different conditions.

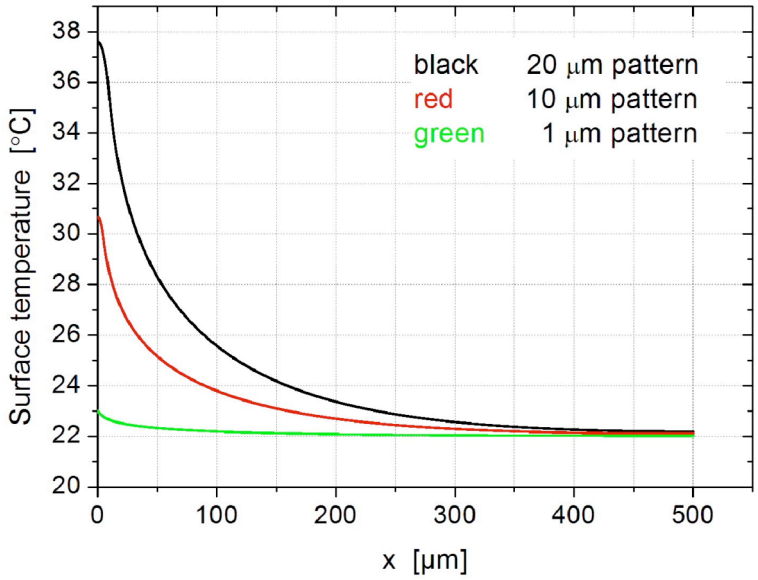

Figure 27: Temperature distribution along the LHC surface in dependence of the illumination width. The model system was a 45 nm thick carbon layer on glass. It was solved for the illumination widths $w/2$ = 0.5; 5; 10 μm after 0.2 s of heating. Q was $3*10^{13}$ W/m^3. The temperature of the top and bottom boundary equaled 22°C.

The kinesin-1 patterning described in the previous chapter was performed at the highest possible laser power. Thus, the experimental set-up and the laser configuration used so far determined the minimal size of the kinesin-1 patterns. Nevertheless, patterns of smaller width can theoretically be realized using higher laser intensities (Fig. 28). Either focusing the laser beam or using a stronger laser for illumination would yield a higher intensity. Creating thin lines using a focused laser beam additionally needs the possibility to scan the beam during patterning. Moreover, in order to achieve a steep temperature gradient the sample has to be cooled.

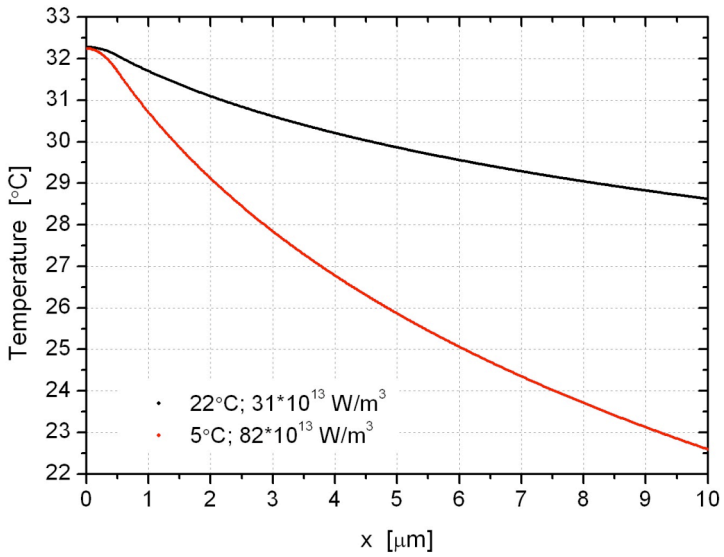

Figure 28: Temperature distribution along the LHC surface for an illumination width of 1 μm in dependence of the patterning conditions. The model system was a 45 nm thick carbon layer on glass. It was solved for different laser intensities and boundary temperatures after 0.2 s of heating. The same temperature was assumed for the top and the bottom boundary. Q was $31*10^{13}$ W/m^3 for $T = 22$°C and $82*10^{13}$ W/m^3 for $T = 5$°C, respectively.

Material-dependent temperature distribution: When solving the model for different LHC materials (Fig. 29) the heat dissipation was of particular interest. Additionally, in one case silicon was chosen as substrate material instead of glass. In order to allow an easy comparison of the materials all conditions besides the material properties (thermal conductivity, heat capacity, density) were identical.

The temperature distributions of carbon and silicon layers are extremely similar (curves lie on top of each other). This was expected since their thermal properties (thermal conductivity and heat capacity, see chapter 7.6) do not differ much. However, although both materials could principally be used for LHC one has to keep in mind that silicon has a lower optical adsorption. For achieving the same amount of heat per volume the laser intensity has to be twice as high as for carbon (at a wavelength of 530 nm, see Figure 22 (page 46). Gold shows a lower local heating and thus a shallower temperature gradient at the edge of the illuminated area but otherwise the temperature distribution is comparable to carbon and silicon. Already at x = 20 µm the curves seem to be identical. Almost no localized heating can be observed if the substrate has a high thermal conductivity like silicon. All theoretical

results qualitatively support experimental observations of 24 nm thick silicon layers on glass, of 15 nm thick gold layers on glass, and of LHC layers on silicon substrates.

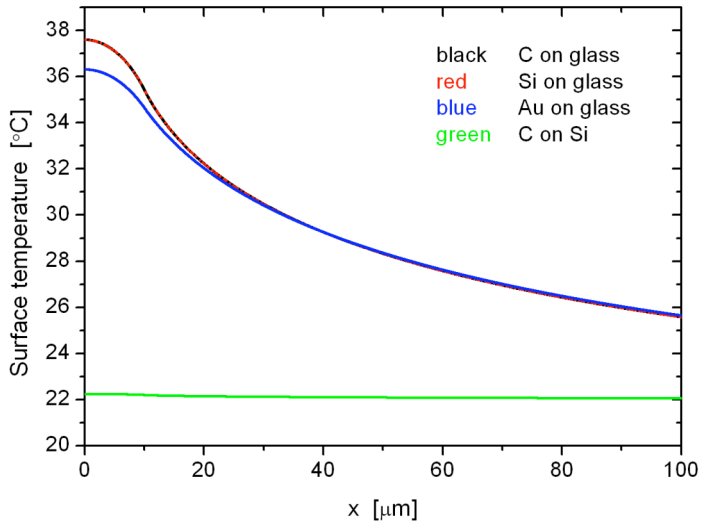

Figure 29: Material-dependent temperature distribution along the surface of a 45 nm thick LHC layer after 0.2 s of heating. The model systems were C on glass, Si on glass, Au on glass as well as C on Si with an illumination width w/2 = 10 μm. Q was $3*10^{13}$ W/m^3. The temperature of the top and bottom boundary equaled 22°C.

In summary, the simulations did show that carbon-glass is a well suited material system for photothermal patterning. High-resolution structures can be theoretically achieved but have yet to be demonstrated experimentally. Besides tuning the patterning conditions by varying the laser intensity, illumination width and temperature, the experimental success will also depend on the actual switching characteristics of PNIPAM, the protein binding dynamics, and the homogeneity of the polymer layer.

5 Outlook: Dual motor patterning of kinesin-1 and axonemal dynein

Surfaces patterned with different motor proteins in a spatially separated manner will offer new possibilities for nanotechnological applications and biophysical investigations. For example, studying the movement of microtubules at a boundary of two opposite polarity motor proteins might be on one hand interesting from a biological point of view but on the other hand could also prove to be useful for molecular sorting applications. The main experimental challenges thereby are to achieve a complete spatial separation of the motors as well as conditions in which both types of motors remain functional.

With respect to this PhD thesis initial experiments with kinesin-1 and 22S dynein (purified in P. Satirs' lab) were performed using μcP. In gliding motility tests, it was observed that casein-coated surfaces blocked dynein motility. Therefore, casein stripes were stamped onto the surface. Afterwards a pure dynein solution was applied to the flow-cell and the motors preferentially absorbed on the surface parts in-between the casein stripes. Kinesin-1 was then allowed to bind to the casein coated areas before motility solution was flown into the cell. However, the motility observations showed that kinesin-1 could, at least to a certain amount, also bind to the areas were dynein motors had been adsorbed. At high kinesin-1 concentrations microtubules were mainly propelled by kinesin-1 motors, as microtubules were gliding with their minus end leading at an average speed of 680±120 nm/s. This is in good agreement with the results of Vale et al. [178] who found that the polarity of microtubule movement is dependent on the kinesin-1 density on the surface if both motors are randomly adsorbed. They further showed that movement in the kinesin-1 direction prevails if the kinesin-1 density is larger than 30 molecules per square micron. After lowering the kinesin-1 concentration in the assay microtubules moving along a kinesin-1-dynein boundary could be observed (Fig. 30). Their plus ends were transported on a kinesin-1 stripe into the minus end direction whereas at the same time the minus ends on a dynein stripe were propelled into the opposite direction. This resulted in a U-shaped movement. However, now microtubules tended to get stuck on the kinesin-1 stripe.

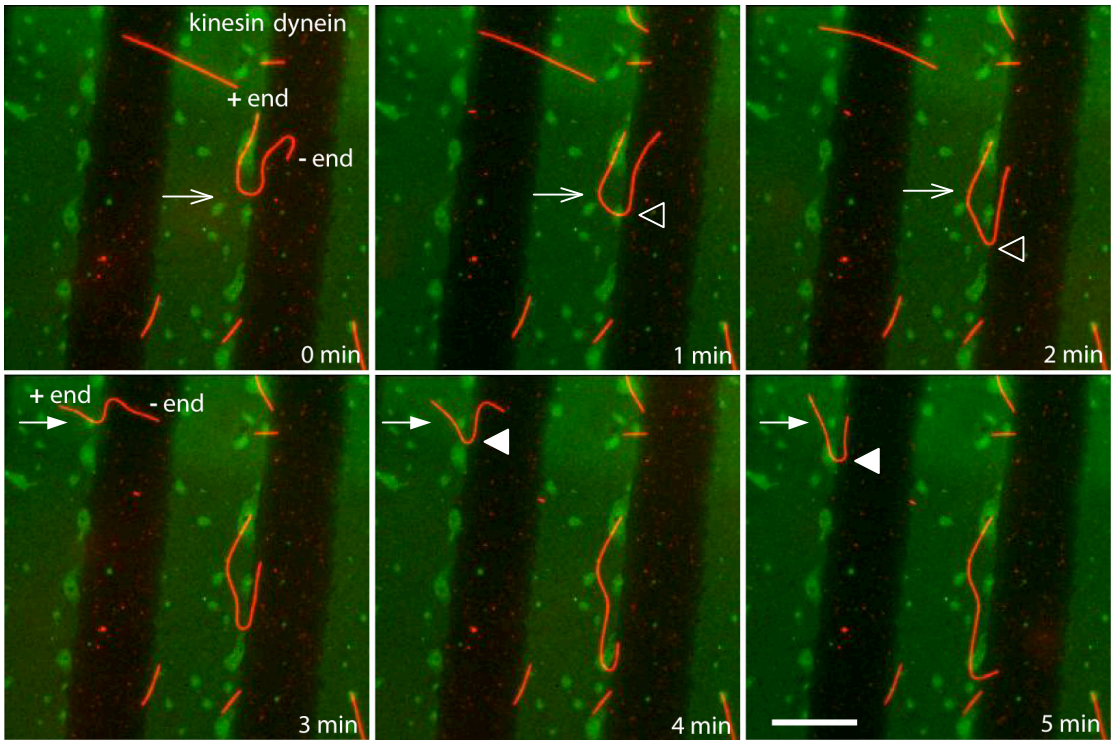

Figure 30: Movement of microtubules at kinesin-1-dynein boundaries. Kinesin-1 (areas with green background; plus-end motor) and dynein motors (dark areas; minus-end motor) where arranged via µcP in stripes on the surface. Fluorescently labeled microtubules (red) moved along the boundary of both motors in a U-shaped manner. The white arrows mark thereby the initial position and the white arrowheads the progression of the microtubule front (open and closed symbols mark two different microtubules). In the course of time the first microtubule got stuck on the kinesin-1 stripe and only the microtubule part on the dynein stripe continued to glide. Scale bar represents 15 µm.

In order to study such effects in more detail, it will be essential to improve the specificity of motor patterning. Substituting casein with streptavidin (and applying biotinylated kinesin-1) or with anti-Penta-His antibodies (and applying his-tagged kinesin-1) in the µcP process was tried but did not achieve this yet. µcP in general might not be appropriate for easy dual motor patterning as direct stamping is not possible. Instead either surface chemistry of the pattern has to specifically support motor activity for one motor type but at the same time completely impede binding of the other motor type.

In contrast, photothermal patterning should be well suited for dual motor patterning. Similar to the sequential patterning of kinesin-1 motors (chapter 4.2) different types of protein can be patterned on the same surface without the need for

specific linker molecules or elaborate surface preparations. Therefore, it will be promising to test this approach in the future.

Concerning the motor type it might be advantageous to employ cytoplasmic dynein instead of axonemal 22S dynein because it moves with about equal velocity (v = 800 nm/s [179]). Thus, ideal U-shaped movement can be expected. However, studying motors with different speeds might reveal other interesting features.

6 Summary

The objective of this work was to pattern planar surfaces with motor proteins in a way that allows controlled and guided movement of microtubule-shuttles. The first part of the work was in particular focused on generating nanometer–sized tracks of motor proteins. The second part explored an in-situ patterning technique for motor proteins to enable user-defined pattern designs, and investigated the achievable resolution.

A novel approach was demonstrated for the nanometer patterning of surfaces with functional motor proteins. The application of biotemplates, namely microtubules, accomplished the highly-localized and oriented surface binding of proteins combined with low protein denaturation by specifically stamping and binding motors. This way functional protein patterns of high surface density were produced.

The generated motor tracks showed that reliable guiding of microtubules without topographical barriers is feasible. Recently, non-topographical patterning of surfaces with kinesin-1 motors was only demonstrated in the micrometer-range. In those experiments it could not be prevented that gliding microtubules walked off the patterned tracks when they approached the boundaries at obtuse angles. Due to the high flexural rigidity of the microtubules the thermal energy of the system was in those cases not sufficient to bend the leading tips of the microtubules back onto the patterned motors. This problem is circumvented by the small width of the motor nanotracks, where the encounters of the microtubules with the boundaries are restricted to extremely shallow angles. Interestingly, tracks of the non-processive motor ncd proved to be even more reliable for guiding and transport on the nanoscale than the kinesin-1 tracks.

Topography-free guiding, as demonstrated in this work, is expected to significantly ease the design and fabrication of microtubule-transport systems and opens up the possibility to transport cargo of unlimited size, i.e. without any constraints by the dimensions of topographic guiding channels. Moreover, the biotemplated patterning is a promising tool for *in vitro* studies on the individual and cooperative action of motor proteins. In particular it might be helpful for the reconstitution of complex subcellular machineries in synthetic environments. As an example, microtubule-microtubule sliding by the biomolecular motor ncd has been

shown to induce directional sliding between antiparallel microtubules and static cross-linking between parallel ones.

Because it was not straightforward to create user-defined motor tracks using the approach of biotemplated patterning, photothermal patterning of functional proteins was established as a new method for freely programmed high-resolution patterning. This way kinesin-1 patterns were generated upon light-induced heating of a light-absorbing layer on the substrate. The surface-grafted poly(N-isopropylacrylamide) (PNIPAM) molecules collapsed locally and allowed motor proteins in solution to bind in the illuminated areas. Microtubule-based gliding motility assays then confirmed the successful patterning of the motors and their functionality since microtubules bound to the patterned kinesin-1 molecules and were transported exclusively in the patterned areas. Besides patterning proteins, localized light-to-heat conversion combined with a surface-grafted thermoresponsive polymer layer was also used for locally activating kinesin-1 molecules and enabling microtubule motility. An advantage of this method is the possibility to use visible light, which is versatile (as many wavelengths can be applied) and non-damaging (in comparison to other recently demonstrated UV-based photopatterning techniques).

Finite element modeling (implemented in COMSOL) showed that light intensity and surface temperature have to be tuned specifically in order to achieve defined pattern sizes. While the currently achieved patterns were in the range of ten micrometers increased optical intensities possibly combined with cooling of the sample allow to significantly scale down the pattern dimensions. However, the eventual experimental resolution will also depend on the switching characteristics of the polymer and the protein binding dynamics.

The produced patterns can be reversibly activated and deactivated at high and low temperature, respectively. Moreover, sequential patterning of multiple kinds of proteins on the same surface will be feasible in a similar way without the need for specific linker molecules or elaborate surface preparation. Further advancements of the technique, as e.g. reconfigurable protein binding for erasing patterns, would certainly improve this approach and its possible applications. Additionally, the development of optically switchable polymers will facilitate motor patterning directly by light and thus ease the method.

7 Materials and Methods

7.1 Microtubules and motor proteins

Microtubules were polymerized from 5 µL of bovine brain tubulin (4 mg/ml; labeled with different fluorophores or biotin as stated below; Cytosceleton Inc.) in Brinkley reassembly buffer (BRB80; 80 mM potassium piperazine-N,N'-bis-(2-ethanesulfonic acid) [PIPES; Sigma], pH 6.9 adjusted with KOH [VWR], 1 mM ethylene glycol-bis (2-aminoethylether)-N,N,N',N'-tetra acetic acid [EGTA; Sigma], 1 mM $MgCl_2$ [VWR]) with 4 mM $MgCl_2$, 1 magnesium mM guanosine triphosphate (Mg-GTP; Roche), and 5% dimethyl-sulfoxide (Sigma) at 37 °C. After 30 min, the microtubule polymers were stabilized and diluted 100-fold in room temperature BRB80 containing 10 µM taxol (Sigma). Polarity marked microtubules were grown as described previuously [180] using bright rhodamine-labeled tubulin for the seeds and dimly rhodamine-labeled tubulin for the elongation.

In the following motor proteins used within this work are listed:

- Wild type kinesin-1 (full length *Drosophila melanogaster*) was expressed in *Escherichia coli* and purified applying a published protocol [39].
- Truncated GFP-labeled *rat* kinesin-1 (GFP-kinesin-1) was expressed in *Escherichia coli* and purified applying a published protocol [181].
- K401-BIO, the biotinylated kinesin-1 derivative, was expressed and purified by D. Drechsel and R. Lemaitre (according to the protocol in [31]) using a plasmid kindly provided by T. Surrey and J. Gelles.
- Ncd (full length *Drosophila melanogaster*, labeled with GFP) was expressed in *Escherichia coli* and purified as described in ref. [154] by L. Hajdo and A.A. Kasprzak (The Nencki Institute of Experimental Biology, Warsaw, Poland).
- *Tetrahymena* 22S dynein was a kind gift of Y. Wada and P. Satir (Albert Einstein College of Medicine, Yeshiva University, New York, USA).

7.2 Preparations of flow-cells for in vitro assays

All experiments were performed in 2-mm-wide and 0.1-mm-high microfluidic flow-cells, self-built from a substrate and a glass coverslip (Corning, No. 1.5) as well as two pieces of double sided sticking tape (3M Scotch) or parafilm (Pechiney) as spacers.

For microtubule-assisted stamping and binding of motor proteins flow-cells were prepared from two glass coverslips (22 × 22 mm^2 and 18 × 18 mm^2). Before use coverslips were either cleaned (sonicated in mucasol (VWR; 1:20 dilution in water) for 15 min, sonicated in ethanol (VWR) for 10 min, rinsed in double distilled water and blown dry with nitrogen, or treated with dichlorodimethylsilane (Sigma) (soaked in a mixture of trichloroethylene (Merck) and dichlorodimethylsilane for 60 min, sonicated in methanol twice, for 5 and 15 min, rinsed in double distilled water and blown dry with nitrogen).

For the photothermal patterning experiments glass coverslips were coated with a light-to-heat converting (LHC) layer: Carbon layers were sputtered in the Fraunhofer IWS by S. Braun and P. Gawlitza. PNIPAM was grafted on silicon wafers and on glass coverslips coated with LHC-layers using atom transfer radical polymerization (ATRP) by L. Ionov according to the procedure described in reference [153]. The glass coverslip on the top side of the sample was pegylated (see reference [182] for PEGylation procedure) to avoid protein binding.

7.3 Biotemplated stamping

Wild type kinesin-1 was mixed with rhodamine labeled microtubules (labeling ratio: 1 rhodamine / 3 unlabeled tubulin units) at a kinesin-1 dimer to tubulin molar ratio of 1:8 in BRB80 buffer containing 1 mM AMPPNP (Sigma) and 10 μM taxol (BRB80TM) to form decorated microtubules. To achieve rapid binding and thus avoid cross-linking of microtubules, the mixing was performed while vortexing the solution. To remove any free, unbound kinesin-1 molecules, 400 μL of the resulting solution (32 nM microtubules, 4 nM kinesin-1 dimers) were centrifuged at 130000g in a Beckmann airfuge for 2.5 min. The pellet was resuspended in 150 μL of BRB80TM.

A 0.5 mg/ml casein (Sigma) solution in BRB80 was perfused into a flow-cell of cleaned glass and allowed to adsorb to the surface for 5 min to reduce the denaturation of kinesin-1 and to prevent the sticking of microtubules. Then the solution containing the decorated microtubules was perfused. After 5 –10 min the flow-cell was washed with BRB80TM containing anti-bleaching reagents (20 mM D-Glucose, 0.020 mg/ml glucose oxidase, 0.008 mg/ml catalase and 1% β-mercaptoethanol [all from Sigma]). To walk the microtubules off the surface an ATP anti-bleaching solution (containing 1mM Mg-ATP [Roche] instead of AMPPNP) was perfused into the cell. In the last step motility solution (microtubules [~30 nM tubulin] in ATP anti-bleaching solution) was added to the cell.

Cargo transport: Rhodamine-biotin labeled transport microtubules (labeling ratio: 3 rhodamine / 4 biotin / 9 unlabeled tubulin units; ~30 nM tubulin) in AMPPNP anti-bleaching solution were perfused into the flow-cell instead of the motility solution. After they had bound to the generated kinesin-1 tracks streptavidin coated quantum dots (525 nm emission, 20000x diluted; Invitrogen) were loaded onto the transport microtubules. Finally an ATP anti-bleaching solution was added to start the movement of the cargo-loaded transport microtubules.

Antibody labeling of the kinesin-1 tracks was performed by perfusing 1.25 µg/ml anti-kinesin (mouse monoclonal SUK4; Cytoskeleton) in PB100BA buffer (100 mM phosphate buffer [Sigma]; pH=7.5 containing 1 mg/ml bovine serum albumin [Merck] and 1 mM ATP) into the flow-cell instead of the motility solution. After one hour incubation the cell was rinsed with PB100BA. FITC-labeled goat anti-mouse IgG (whole molecule; 17 µg/ml in PB100BA; Sigma-Aldrich) was added as secondary antibody. After another 45 minutes of incubation, the solution was exchanged with an ATP anti-bleaching solution.

Evaluation of kinesin-1 decoration: Microtubules were immobilized on a hydrophobic glass surface via anti-beta-tubulin antibodies as described for kinesin-1 binding in chapter 6.4. Before and after incubating GFP-labeled kinesin-1 solutions (0.325 nM – 26 nM in BRB80TM) for 10 min the flow-cell was rinsed with BRB80TM containing anti-bleaching reagents. Microtubules decorated with GFP-labeled kinesin-1 in solution (procedure as described above) were bound to a cleaned glass surface previously coated with anti-Penta-His antibodies (10 µg/ml; Qiagen) and casein. The sample was then washed with BRB80TM containing anti-bleaching

reagents. To be able to compare the fluorescent intensity of different microtubules in a field of view with uneven illumination TIRF (total internal reflection fluorescence) images were taken of both, the fluorescence of GFP and rhodamine. The rhodamine fluorescence, which was assumed to be equal for different microtubules, was then used to determine a relative intensity of the GFP fluorescence according to the following formula:

$$I^{\text{GFP}}_{\text{relative}} = \frac{I^{\text{GFP}}_{\text{measured}} - I^{\text{GFP}}_{\text{background}}}{I^{\text{rhodamine}}_{\text{measured}} - I^{\text{rhodamine}}_{\text{background}}}. \qquad \text{(Equation 11)}$$

7.4 Biotemplated binding (and ncd sliding)

Kinesin-1 binding: Anti-beta-tubulin (TUB 2.1, 4 μg/ml; Sigma) or anti-tetramethylrhodamine (4 μg/ml; Molecular Probes) antibodies were adsorbed for 5 min onto a hydrophobic glass surface that was previously treated with dichlorodimethylsilane. The surface was then blocked against unspecific protein binding by Pluronic F127 (1% dissolved in BRB80, Sigma). Rhodamine-biotin labeled microtubules (labeling ratio: 3 rhodamine / 4 biotin / 9 unlabeled tubulin units) were polymerized, and unpolymerized tubulin was removed by 5 min centrifugation at 180000g in a Beckmann airfuge. The pellet was resuspended in BRB80 containing 10 μM taxol to a final tubulin concentration of 80 nM. This solution was added to the flow-cell in order to bind these template microtubules to the antibodies on the substrate surface. In the next steps, first fluorescein labeled streptavidin (10 μg/ml in BRB80, Pierce) was perfused into the flow-cell. Secondly, biotinylated kinesin-1 K401-BIO (2.5 μg/ml in BRB80, containing 10 μM taxol, 0.5 mg/ml casein and 20 mM ATP) was added. The flow-cell was rinsed with ATP anti-bleaching solution and microtubule containing motility solution (chapter 6.3) was perfused. In experiments with anti-tubulin antibodies free tubulin was added to the motility solution with a final concentration of 20 μg/ml. In experiments where anti-tetramethylrhodamine antibodies were used to immobilize template microtubules the transport microtubules were labeled with Alexa-488.

Ncd binding: Anti-Penta-His antibodies (10 µg/ml; Qiagen) were adsorbed onto the hydrophobic glass surface of the flow-cell. After blocking the surface with Pluronic F127 (1% dissolved in BRB80), his-tagged kinesin-1 was bound to these

antibodies. Dimly rhodamine-labeled microtubules (labeling ratio: 1 rhodamine / 5 unlabeled tubulin units) in BRB80TM were then immobilized on the kinesin-1-coated surface. To remove the unbound microtubules, the flow-cell was rinsed with BRB80TM. Bound microtubules were crosslinked for 15 min in a 0.1% solution of glutaraldehyde (Sigma) in BRB80TM. Subsequently, a 15 min treatment of the cell with 0.1 M glycine (Merck) was performed to block free aldehyde groups.

Ncd was diluted in BRB20 buffer (20 mM potassium PIPES, pH 6.9 adjusted with KOH, 1 mM EGTA, 1 mM $MgCl_2$) containing 10 µM taxol, 1 mM ATP and 100 mM NaCl. This solution was centrifuged for 5 min at 180000g in a Beckmann airfuge to remove clustered molecules and then added to the fixed microtubules in the flow-cell. Finally, after washing twice with BRB20 containing 10 µM taxol and 1 mM ATP, motility solution containing microtubules (~30 nM tubulin) and ATP anti-bleaching solution (in BRB20) was flown in.

Directional sliding of ncd: After performing a ncd binding experiment ncd and ATP anti-bleaching solution was added to the flow-cell. The polarity of the template microtubules was revealed either by immobilizing polarity marked microtubules or by applying GFP-kinesin-1 as described in [166]. The interaction of ncd molecules with immobilized microtubules was imaged before flowing in motility solution in a ncd binding experiment.

7.5 Photothermal patterning

The back of the sample (in case of glass samples only) was colored with black permanent marker to block the autofluorescence of the thermal contact. The sample was then mounted on a peltier with heat transfer compound for keeping it at defined temperature. The peltier was coupled to a power supply and a thermometer (Physitemp BAT-10).

Kinesin-1 gliding motility assay: A casein-containing solution (0.5 mg/ml in BRB80) was perfused into the flow-cell and allowed to adsorb to the surface for 5 min. Then a 10 μg/ml kinesin-1 solution in BRB80 buffer containing 1mM Mg-ATP and 0.2 mg/ml casein (BRB80CA) was perfused. After 5 – 10 min motility solution (chapter 6.3) was added to the cell.

Patterning of kinesin-1: The PNIPAM sample was kept at low temperature (15-25°C). A kinesin-1 solution (20 μg/ml) containing 0.5 mg/ml casein and anti-

bleaching reagents in BRB80 was perfused into the flow-cell. The sample was then locally illuminated through a 63x water immersion objective (Zeiss, numerical aperture NA=1.2) for 2 min using a collimated laser beam (wavelength = 530 nm, green line) with parallel light and different aperture openings. After patterning non-adsorbed protein was removed by multiple perfusions with BRB80CA. In the next step motility solution was added to the cell and the temperature was raised to 35°C.

7.6 Finite element modeling

The modeling of the heat distribution during photohtermal patterning was performed using the software COMSOL Multiphysics Version 3.4. Besides the 2D model of the experimental system and the conditions and equations described in chapter 4.3 the following parameters and settings were applied:

- Mesh size: extra coarse
- Linear system solver: direct solver UMFPACK
- Time dependent solver: 200 ms in 10 ms steps

The material properties relevant for heat transfer by conduction are listed in table 3.

Material	Thermal conductivity k [W/(m*K)]	Heat capacity at constant pressure C_p [J/(kg*K)]	Density ρ [kg/m^3]
carbon (graphite)	150	710	1950
gold	314	130	19300
silica glass	1.38	703	2203
silicon	148	741	2330
water	0.6	4182	9982

Table 3: Properties of substrate and LHC materials.

The initial temperature was chosen for all subdomains to always equal the temperature of the boundary on the bottom of the model (peltier temperature). The boundary on the top was set to 22°C.

7.7 Dual motor patterning

PDMS stamps were prepared by pouring a mix of 10 parts silicone elastomer and 1 part cross linking agent from a Sylgard 184 Silicone elastomer Kit (Dow Corning) on the silicon master, and baking it at 60°C for 4 hours. A casein solution (0.8 mg/ml casein and 0.2 mg/ml FITC-casein in BRB80) was incubated for 10 to 15 min on the stamp. After immersing the stamp in BRB80 as well as in nanopure water it was blown dry with nitrogen and subsequently brought into contact with the cleaned glass substrate for printing the casein molecules. Then the flow-cell was assembled and the surface was washed with the 22S dynein specific motility buffer DMB (10 mM tris(hydroxymethyl)-aminomethan (TRIS) acetate [Sigma], 3 mM $MgSO_4$ [Merck], 2 mM EGTA (pH 7.5)), supplemented with 2 mM dithiothreitol (DTT; Sigma) and 50 mM potassium acetate (Merck). The washing was repeated twice, after perfusing dynein (100 μg/ml) and allowing it to bind for 2 min as well as after 2 min of incubating a 3.5 μg/ml kinesin-1 solution in DMB. Then the flow-cell content was exchanged with a 1 mg/ml casein solution in DMB, which was after another 2 min finally washed out with a motility solution (DMB buffer instead of BRB80).

7.8 Data acquisition and analysis

Fluorescent images were obtained using an inverted optical microscope (Zeiss Axiovert 200M) with a 100x oil immersion objective NA = 1.3, a 100x oil immersion objective NA 1.46 (for total internal reflection fluorescence microscopy) or a 63x water immersion objective NA = 1.2 (for photohermal patterning experiments). For excitation a Lumen 200 metal arc lamp (Prior Scientific Instruments Ltd.) was used. An argon-krypton mixed gas laser (Coherent Innova 70C Spectra) at 488 nm was applied for total internal reflection fluorescence microscopy. The green line (530 nm) of the same laser was used for locally activating and patterning motors. For data acquisition a back-illuminated charge coupled device camera (MicroMax 512 BFT, Roper Scientific) was used in conjunction with a Metamorph imaging system (Universal Imaging Corp., Downington, PA). The used tetramethylrhodamine-isothiocyanate (TRITC), FITC and GFP filters were from Chroma Technology. Images were acquired every 1 s with an exposure time of 100 ms unless stated otherwise.

Automated tracking of motile microtubules was performed using an inhouse software based on MatLab (Mathworks, Natick, MA). The applied fitting algorithm used Gaussian-based model functions.

Bibliography

1. Lowe, C.R. (2000). Nanobiotechnology: the fabrication and applications of chemical and biological nanostructures. Current Opinion in Structural Biology *10*, 428-434.

2. Drexler, K.E. (1981). Molecular Engineering - an Approach to the Development of General Capabilities for Molecular Manipulation. Proceedings of the National Academy of Sciences of the United States of America-Physical Sciences *78*, 5275-5278.

3. Drexler, K.E. (1999). Building molecular machine systems. Trends in Biotechnology *17*, 5-7.

4. Hess, H., and Vogel, V. (2001). Molecular shuttles based on motor proteins: active transport in synthetic environments. J Biotechnol *82*, 67-85.

5. Merkle, R.C. (1999). Biotechnology as a route to nanotechnology. Trends in Biotechnology *17*, 271-274.

6. Browne, W.R., and Feringa, B.L. (2006). Making molecular machines work. Nat Nanotechnol *1*, 25-35.

7. van den Heuvel, M.G.L., and Dekker, C. (2007). Motor proteins at work for nanotechnology. Science *317*, 333-336.

8. Soong, R.K., Bachand, G.D., Neves, H.P., Olkhovets, A.G., Craighead, H.G., and Montemagno, C.D. (2000). Powering an inorganic nanodevice with a biomolecular motor. Science *290*, 1555-1558.

9. Goel, A., and Vogel, V. (2008). Harnessing biological motors to engineer systems for nanoscale transport and assembly. Nature Nanotechnology *3*, 465-475.

10. Hess, H., Bachand, G.D., and Vogel, V. (2004). Powering nanodevices with biomolecular motors. Chemistry-a European Journal *10*, 2110-2116.

11. Cheng, L.J., Kao, M.T., Meyhofer, E., and Guo, L.J. (2005). Highly efficient guiding of microtubule transport with imprinted CYTOP nanotracks. Small *1*, 409-414.

12. Clemmens, J., Hess, H., Doot, R., Matzke, C.M., Bachand, G.D., and Vogel, V. (2004). Motor-protein "roundabouts": Microtubules moving on kinesin-coated tracks through engineered networks. Lab on a Chip *4*, 83-86.

13. Hess, H., Matzke, C.M., Doot, R.K., Clemmens, J., Bachand, G.D., Bunker, B.C., and Vogel, V. (2003). Molecular shuttles operating undercover: A new photolithographic approach for the fabrication of structured surfaces supporting directed motility. Nano Letters *3*, 1651-1655.

14. Huang, Y.M., Uppalapati, M., Hancock, W.O., and Jackson, T.N. (2005). Microfabricated capped channels for biomolecular motor-based transport. Ieee Transactions on Advanced Packaging *28*, 564-570.

15. van den Heuvel, M.G.L., Butcher, C.T., Smeets, R.M.M., Diez, S., and Dekker, C. (2005). High rectifying efficiencies of microtubule motility on kinesin-coated gold nanostructures. Nano Letters *5*, 1117-1122.

16. Hiratsuka, Y., Tada, T., Oiwa, K., Kanayama, T., and Uyeda, T.Q.P. (2001). Controlling the direction of kinesin-driven microtubule movements along microlithographic tracks. Biophysical Journal *81*, 1555-1561.

17. Hess, H., Clemmens, J., Matzke, C.M., Bachand, G.D., Bunker, B.C., and Vogel, V. (2002). Ratchet patterns sort molecular shuttles. Applied Physics a (Materials Science Processing) *A75*, 309-313.

18. Lipscomb, R.C., Clemmens, J., Hanein, Y., Holl, M.R., Vogel, V., Ratner, B.D., Denton, D.D., Bohringer, K.F. (2002). Controlled microtubules transport on patterned non-fouling surfaces. 2nd Annual International IEEE-EMB Special Topic Conference on Microtechnologies in Medicine & Biology, 21-26.

19. Clemmens, J., Hess, H., Lipscomb, R., Hanein, Y., Bohringer, K.F., Matzke, C.M., Bachand, G.D., Bunker, B.C., and Vogel, V. (2003). Mechanisms of microtubule guiding on microfabricated kinesin-coated surfaces: Chemical and topographic surface patterns. Langmuir *19*, 10967-10974.

20. Bernard, A., Renault, J.P., Michel, B., Bosshard, H.R., and Delamarche, E. (2000). Microcontact printing of proteins. Advanced Materials *12*, 1067-1070.

21. Ginger, D.S., Zhang, H., and Mirkin, C.A. (2004). The evolution of dip-pen nanolithography. Angewandte Chemie-International Edition *43*, 30-45.

22. Lee, K.B., Lim, J.H., and Mirkin, C.A. (2003). Protein nanostructures formed via direct-write dip-pen nanolithography. Journal of the American Chemical Society *125*, 5588-5589.

23. Lim, J.H., Ginger, D.S., Lee, K.B., Heo, J., Nam, J.M., and Mirkin, C.A. (2003). Direct-write dip-pen nanolithography of proteins on modified silicon oxide surfaces. Angewandte Chemie-International Edition *42*, 2309-2312.

24. Wilson, D.L., Martin, R., Hong, S., Cronin-Golomb, M., Mirkin, C.A., and Kaplan, D.L. (2001). Surface organization and nanopatterning of collagen by dip-pen nanolithography. Proceedings of the National Academy of Sciences of the United States of America *98*, 13660-13664.

25. Graber, D.J., Zieziulewicz, T.J., Lawrence, D.A., Shain, W., and Turner, J.N. (2003). Antigen binding specificity of antibodies patterned by microcontact printing. Langmuir *19*, 5431-5434.

26. Alberts, B., Johnson, A., Lewis, J., Raff, M., Roberts, K., Walter, P. (2002). Molecular biology of the cell, (New York: Garland Science).

27. Wade, R.H., Meurer-Grob, P., Metoz, F., and Arnal, I. (1998). Organisation and structure of microtubules and microtubule-motor protein complexes. European Biophysics Journal with Biophysics Letters *27*, 446-454.

28. Howard, J. (2001). Mechanics of motor proteins and the cytosceleton, (Sinauer Associates, Sunderland, MA).

29. Brady, S.T. (1985). A Novel Brain Atpase with Properties Expected for the Fast Axonal-Transport Motor. Nature *317*, 73-75.

30. Vale, R.D., Reese, T.S., and Sheetz, M.P. (1985). Identification of a Novel Force-Generating Protein, Kinesin, Involved in Microtubule-Based Motility. Cell *42*, 39-50.

31. Berliner, E., Young, E.C., Anderson, K., Mahtani, H.K., and Gelles, J. (1995). Failure of a single-headed kinesin to track parallel to microtubule protofilaments. Nature *373*, 718-721.

32. Gilbert, S.P., Webb, M.R., Brune, M., and Johnson, K.A. (1995). Pathway of Processive Atp Hydrolysis by Kinesin. Nature *373*, 671-676.

33. Hackney, D.D. (1995). Highly Processive Microtubule-Stimulated Atp Hydrolysis by Dimeric Kinesin Head Domains. Nature *377*, 448-450.

34. Howard, J. (1996). The movement of kinesin along microtubules. Annual Review of Physiology *58*, 703-729.

35. Asbury, C.L., Fehr, A.N., and Block, S.M. (2003). Kinesin moves by an asymmetric hand-over-hand mechanism. Science *302*, 2130-2134.

36. Kaseda, K., Higuchi, H., and Hirose, K. (2003). Alternate fast and slow stepping of a heterodimeric kinesin molecule. Nature Cell Biology *5*, 1079-1082.

37. Schief, W.R., Clark, R.H., Crevenna, A.H., and Howard, J. (2004). Inhibition of kinesin motility by ADP and phosphate supports a hand-over-hand mechanism. Proceedings of the National Academy of Sciences of the United States of America *101*, 1183-1188.

38. Yildiz, A., Tomishige, M., Vale, R.D., and Selvin, P.R. (2004). Kinesin walks hand-over-hand. Science *303*, 676-678.

39. Coy, D.L., Wagenbach, M., and Howard, J. (1999). Kinesin takes one 8-nm step for each ATP that it hydrolyzes. J Biol Chem *274*, 3667-3671.

40. Schnitzer, M.J., and Block, S.M. (1997). Kinesin hydrolyses one ATP per 8-nm step. Nature *388*, 386-390.

41. Svoboda, K., Schmidt, C.F., Schnapp, B.J., and Block, S.M. (1993). Direct Observation of Kinesin Stepping by Optical Trapping Interferometry. Nature *365*, 721-727.

42. Gelles, J., Schnapp, B.J., and Sheetz, M.P. (1988). Tracking Kinesin-Driven Movements with Nanometre-Scale Precision. Nature *331*, 450-453.

43. Ray, S., Meyhofer, E., Milligan, R.A., and Howard, J. (1993). Kinesin Follows the Microtubules Protofilament Axis. J Cell Biol *121*, 1083-1093.

44. Bohm, K.J., Stracke, R., and Unger, E. (2000). Speeding up kinesin-driven microtubule gliding in vitro by variation of cofactor composition and physicochemical parameters. Cell Biology International *24*, 335-341.

45. Diez, S., Helenius, J.H., Howard, J. (2004). Biomolecular motors operating in engineered environments. In Nanobiotechnology: Concepts, Applications and Perspectives, C.M. Niemeyer, Mirkin, C.A., ed. (Weinheim: Wiley-VCH), pp. 185-199.

46. Meyhofer, E., and Howard, J. (1995). The Force Generated by a Single Kinesin Molecule against an Elastic Load. Proceedings of the National Academy of Sciences of the United States of America *92*, 574-578.

47. Svoboda, K., and Block, S.M. (1994). Force and Velocity Measured for Single Kinesin Molecules. Cell *77*, 773-784.

48. Visscher, K., Schnitzer, M.J., and Block, S.M. (1999). Single kinesin molecules studied with a molecular force clamp. Nature *400*, 184-189.

49. Woehlke, G., and Schliwa, M. (2000). Walking on two heads: The many talents of kinesin. Nature Reviews Molecular Cell Biology *1*, 50-58.

50. Mcdonald, H.B., Stewart, R.J., and Goldstein, L.S.B. (1990). The Kinesin-Like Ncd Protein of Drosophila Is a Minus End-Directed Microtubule Motor. Cell *63*, 1159-1165.

51. Walker, R.A., Salmon, E.D., and Endow, S.A. (1990). The Drosophila-Claret Segregation Protein Is a Minus-End Directed Motor Molecule. Nature *347*, 780-782.

52. Hatsumi, M., and Endow, S.A. (1992). Mutants of the Microtubule Motor Protein, Nonclaret Disjunctional, Affect Spindle Structure and Chromosome Movement in Meiosis and Mitosis. Journal of Cell Science *101*, 547-559.

53. Saunders, W.S., and Hoyt, M.A. (1992). Kinesin-Related Proteins Required for Structural Integrity of the Mitotic Spindle. Cell *70*, 451-458.

54. Matthies, H.J.G., McDonald, H.B., Goldstein, L.S.B., and Theurkauf, W.E. (1996). Anastral meiotic spindle morphogenesis: Role of the non-claret disjunctional kinesin-like protein. J Cell Biol *134*, 455-464.

55. Skold, H.N., Komma, D.J., and Endow, S.A. (2005). Assembly pathway of the anastral Drosophila oocyte meiosis I spindle. Journal of Cell Science *118*, 1745-1755.

56. Chandra, R., Salmon, E.D., Erickson, H.P., Lockhart, A., and Endow, S.A. (1993). Structural and Functional Domains of the Drosophila Ncd Microtubule Motor Protein. J Biol Chem *268*, 9005-9013.

57. Karabay, A., and Walker, R.A. (1999). Identification of microtubule binding sites in the Ncd tail domain. Biochemistry *38*, 1838-1849.

58. Sablin, E.P., Case, R.B., Dai, S.C., Hart, C.L., Ruby, A., Vale, R.D., and Fletterick, R.J. (1998). Direction determination in the minus-end-directed kinesin motor ncd. Nature *395*, 813-816.

59. Case, R.B., Pierce, D.W., HomBooher, N., Hart, C.L., and Vale, R.D. (1997). The directional preference of kinesin motors is specified by an element outside of the motor catalytic domain. Cell *90*, 959-966.

60. Endow, S.A., and Higuchi, H. (2000). A mutant of the motor protein kinesin that moves in both directions on microtubules. Nature *406*, 913-916.

61. Endow, S.A., and Waligora, K.W. (1998). Determinants of kinesin motor polarity. Science *281*, 1200-1202.

62. Henningsen, U., and Schliwa, M. (1997). Reversal in the direction of movement of a molecular motor. Nature *389*, 93-96.

63. Schliwa, M., and Woehlke, G. (2003). Molecular motors. Nature *422*, 759-765.

64. deCastro, M.J., Ho, C.H., and Stewart, R.J. (1999). Motility of dimeric ncd on a metal-chelating surfactant: Evidence that ncd is not processive. Biochemistry-Us *38*, 5076-5081.

65. Furuta, K., and Toyoshima, Y.Y. (2008). Minus-end-directed motor ncd exhibits processive movement that is enhanced by microtubule bundling in vitro. Current Biology *18*, 152-157.

66. deCastro, M.J., Fondecave, R.M., Clarke, L.A., Schmidt, C.F., and Stewart, R.J. (2000). Working strokes by single molecules of the kinesin-related microtubule motor ncd. Nature Cell Biology *2*, 724-729.

67. Foster, K.A., and Gilbert, S.P. (2000). Kinetic studies of dimeric Ncd: Evidence that Ncd is not processive. Biochemistry *39*, 1784-1791.

68. Gibbons, I.R., and Rowe, A.J. (1965). Dynein - a Protein with Adenosine Triphosphatase Activity from Cilia. Science *149*, 424-426.

69. Oiwa, K., and Sakakibara, H. (2005). Recent progress in dynein structure and mechanism. Current Opinion in Cell Biology *17*, 98-103.

70. Vale, R.D., and Toyoshima, Y.Y. (1988). Rotation and Translocation of Microtubules Invitro Induced by Dyneins from Tetrahymena Cilia. Cell *52*, 459-469.

71. Hirakawa, E., Higuchi, H., and Toyoshima, Y.Y. (2000). Processive movement of single 22S dynein molecules occurs only at low ATP concentrations. Proceedings of the National Academy of Sciences of the United States of America *97*, 2533-2537.

72. Kinosita, K., Yasuda, R., Noji, H., and Adachi, K. (2000). A rotary molecular motor that can work at near 100% efficiency. Philosophical Transactions of the Royal Society of London Series B-Biological Sciences *355*, 473-489.

73. Bohm, K.J., Stracke, R., Muhlig, P., and Unger, E. (2001). Motor protein-driven unidirectional transport of micrometer-sized cargoes across isopolar microtubule arrays. Nanotechnology *12*, 238-244.

74. Limberis, L., and Stewart, R.J. (2000). Toward kinesin-powered microdevices. IOP Publishing. Nanotechnology *11*, 47-51.

75. Muthukrishnan, G., Hutchins, B.M., Williams, M.E., and Hancock, W.O. (2006). Transport of semiconductor nanocrystals by kinesin molecular motors. Small *2*, 626-630.

76. Brown, T.B., and Hancock, W.O. (2002). A polarized microtubule array for kinesin-powered-nanoscale assembly and force generation. Nano Letters *2*, 1131-1135.

77. Doot, R.K., Hess, H., and Vogel, V. (2007). Engineered networks of oriented microtubule filaments for directed cargo transport. Soft Matter *3*, 349-356.

78. Block, S.M., Goldstein, L.S.B., and Schnapp, B.J. (1990). Bead Movement by Single Kinesin Molecules Studied with Optical Tweezers. Nature *348*, 348-352.

79. Howard, J., Hudspeth, A.J., and Vale, R.D. (1989). Movement of Microtubules by Single Kinesin Molecules. Nature *342*, 154-158.

80. Hess, H. (2006). Self-assembly driven by molecular motors. Soft Matter *2*, 669-677.

81. Diez, S., Reuther, C., Dinu, C., Seidel, R., Mertig, M., Pompe, W., and Howard, J. (2003). Stretching and transporting DNA molecules using motor proteins. Nano Lett *3*, 1251-1254.

82. Dinu, C.Z., Opitz, J., Pompe, W., Howard, J., Mertig, M., and Diez, S. (2006). Parallel manipulation of bifunctional DNA molecules on structured surfaces using kinesin-driven microtubules. Small *2*, 1090-1098.

83. Hess, H., Howard, J., and Vogel, V. (2002). A piconewton forcemeter assembled from microtubules and kinesins. Nano Letters *2*, 1113-1115.

84. Hess, H., Clemmens, J., Howard, J., and Vogel, V. (2002). Surface imaging by self-propelled nanoscale probes. Nano Letters *2*, 113-116.

85. Bachand, G.D., Rivera, S.B., Carroll-Portillo, A., Hess, H., and Bachand, M. (2006). Active capture and transport of virus particles using a biomolecular motor-driven, nanoscale antibody sandwich assay. Small *2*, 381-385.

86. Bachand, G.D., Rivera, S.B., Boal, A.K., Gaudioso, J., Liu, J., and Bunker, B.C. (2004). Assembly and transport of nanocrystal CdSe quantum dot nanocomposites using microtubules and kinesin motor proteins. Nano Letters *4*, 817-821.

87. Hess, H., Clemmens, J., Qin, D., Howard, J., and Vogel, V. (2001). Light-controlled molecular shuttles made from motor proteins carrying cargo on engineered surfaces. Nano Letters *1*, 235-239.

88. Ramachandran, S., Ernst, K.H., Bachand, G.D., Vogel, V., and Hess, H. (2006). Selective loading of kinesin-powered molecular shuttles with protein cargo and its application to biosensing. Small *2*, 330-334.

89. Brunner, C., Wahnes, C., and Vogel, V. (2007). Cargo pick-up from engineered loading stations by kinesin driven molecular shuttles. Lab on a Chip *7*, 1263-1271.

90. Lin, C.T., Kao, M.T., Kurabayashi, K., and Meyhofer, E. (2008). Self-contained biomolecular motor-driven protein sorting and concentrating in an ultrasensitive microfluidic chip. Nano Letters *8*, 1041-1046.

91. van den Heuvel, M.G.L., De Graaff, M.P., and Dekker, C. (2006). Molecular sorting by electrical steering of microtubules in kinesin-coated channels. Science *312*, 910-914.

92. Kerssemakers, J., Howard, J., Hess, H., and Diez, S. (2006). The distance that kinesin-1 holds its cargo from the microtubule surface measured by fluorescence interference contrast microscopy. Proceedings of the National Academy of Sciences of the United States of America *103*, 15812-15817.

93. Nitzsche, B., Ruhnow, F., and Diez, S. (2008). Quantum-dot-assisted characterization of microtubule rotations during cargo transport. Nature Nanotechnology *3*, 552-556.

94. Gast, F.U., Dittrich, P.S., Schwille, P., Weigel, M., Mertig, M., Opitz, J., Queitsch, U., Diez, S., Lincoln, B., Wottawah, F., et al. (2006). The microscopy cell (MicCell), a versatile modular flowthrough system for cell biology, biomaterial research, and nanotechnology. Microfluidics and Nanofluidics *2*, 21-36.

95. Tucker, R., Katira, P., and Hess, H. (2008). Herding nanotransporters: Localized activation via release and sequestration of control molecules. Nano Letters *8*, 221-226.

96. Hutchins, B.M., Platt, M., Hancock, W.O., and Williams, M.E. (2007). Directing transport of CoFe2O4-functionalized microtubules with magnetic fields. Small *3*, 126-131.

97. Stracke, P., Bohm, K.J., Burgold, J., Schacht, H.J., and Unger, E. (2000). Physical and technical parameters determining the functioning of a kinesin-based cell-free motor system. IOP Publishing. Nanotechnology *11*, 52-56.

98. Dennis, J.R., Howard, J., and Vogel, V. (1999). Molecular shuttles: directed motion of microtubules slang nanoscale kinesin tracks. Nanotechnology *10*, 232-236.

99. Moorjani, S.G., Jia, L., Jackson, T.N., and Hancock, W.O. (2003). Lithographically Patterned Channels Spatially Segregate Kinesin Motor Activity and Effectively Guide Microtubule Movements. Nano Lett *3*, 633 -637.

100. Clemmens, J., Hess, H., Howard, J., and Vogel, V. (2003). Analysis of microtubule guidance in open microfabricated channels coated with the motor protein kinesin. Langmuir *19*, 1738-1744.

101. Nitta, T., Tanahashi, A., Obara, Y., Hirano, M., Razumova, M., Regnier, M., and Hess, H. (2008). Comparing guiding track requirements for myosin- and kinesin-powered molecular shuttles. Nano Letters *8*, 2305-2309.

102. Mansson, A., Sundberg, M., Bunk, R., Balaz, M., Nicholls, I.A., Omling, P., Tegenfeldt, J.O., Tagerud, S., and Montelius, L. (2005). Actin-based molecular motors for cargo transportation in nanotechnology - Potentials and challenges. Ieee Transactions on Advanced Packaging *28*, 547-555.

103. Folch, A., and Toner, M. (2000). Microengineering of cellular interactions. Annual Review of Biomedical Engineering *2*, 227-256.

104. Khademhosseini, A., Langer, R., Borenstein, J., and Vacanti, J.P. (2006). Microscale technologies for tissue engineering and biology. Proceedings of the National Academy of Sciences of the United States of America *103*, 2480-2487.

105. Li, N., Tourovskaia, A., Folch, A. (2003). Biology on a chip: microfabrication for studying the behavior of cultured cells. Critical reviews in biomedical engineering *31(5-6)*, 423-488.

106. Raghavan, S., and Chen, C.S. (2004). Micropatterned environments in cell biology. Advanced Materials *16*, 1303-1313.

107. Sniadecki, N., Desai, R.A., Ruiz, S.A., and Chen, C.S. (2006). Nanotechnology for cell-substrate interactions. Annals of Biomedical Engineering *34*, 59-74.

108. Babacan, S., Pivarnik, P., Letcher, S., and Rand, A.G. (2000). Evaluation of antibody immobilization methods for piezoelectric biosensor application. Biosensors & Bioelectronics *15*, 615-621.

109. MacBeath, G., and Schreiber, S.L. (2000). Printing proteins as microarrays for high-throughput function determination. Science *289*, 1760-1763.

110. Senaratne, W., Andruzzi, L., and Ober, C.K. (2005). Self-assembled monolayers and polymer brushes in biotechnology: Current applications and future perspectives. Biomacromolecules *6*, 2427-2448.

111. Kumar, A., and Whitesides, G.M. (1993). Features of Gold Having Micrometer to Centimeter Dimensions Can Be Formed through a Combination of Stamping with an Elastomeric Stamp and an Alkanethiol Ink Followed by Chemical Etching. Applied Physics Letters *63*, 2002-2004.

112. Odom, T.W., Love, J.C., Wolfe, D.B., Paul, K.E., and Whitesides, G.M. (2002). Improved pattern transfer in soft lithography using composite stamps. Langmuir *18*, 5314-5320.

113. Renault, J.P., Bernard, A., Bietsch, A., Michel, B., Bosshard, H.R., Delamarche, E., Kreiter, M., Hecht, B., and Wild, U.P. (2003). Fabricating Arrays of Single Protein Molecules on Glass Using Microcontact Printing. The Journal of Physical Chemistry B *107*, 703-711.

114. Piner, R.D., Zhu, J., Xu, F., Hong, S.H., and Mirkin, C.A. (1999). "Dip-pen" nanolithography. Science *283*, 661-663.

115. Demers, L.M., Ginger, D.S., Park, S.J., Li, Z., Chung, S.W., and Mirkin, C.A. (2002). Direct patterning of modified oligonucleotides on metals and insulators by dip-pen nanolithography. Science *296*, 1836-1838.

116. Vega, R.A., Maspoch, D., Salaita, K., and Mirkin, C.A. (2005). Nanoarrays of single virus particles. Angewandte Chemie-International Edition *44*, 6013-6015.

117. Salaita, K., Lee, S.W., Wang, X.F., Huang, L., Dellinger, T.M., Liu, C., and Mirkin, C.A. (2005). Sub-100 nm, centimeter-scale, parallel dip-pen nanolithography. Small *1*, 940-945.

118. Tinazli, A., Piehler, J., Beuttler, M., Guckenberger, R., and Tampe, R. (2007). Native protein nanolithography that can write, read and erase. Nature Nanotechnology *2*, 220-225.

119. Blawas, A.S., and Reichert, W.M. (1998). Protein patterning. Biomaterials *19*, 595-609.

120. Matsuda, T., and Sugawara, T. (1995). Photochemical Protein Fixation on Polymer Surfaces Via Derivatized Phenyl Azido Group. Langmuir *11*, 2272-2276.

121. Nivens, D.A., and Conrad, D.W. (2002). Photoactive poly(ethylene glycol) organosilane films for site-specific protein immobilization. Langmuir *18*, 499-504.

122. Yang, Z.P., Frey, W., Oliver, T., and Chilkoti, A. (2000). Light-activated affinity micropatterning of proteins on self-assembled monolayers on gold. Langmuir *16*, 1751-1758.

123. Wilde, L.M., Farace, G., Roberts, C.J., Davies, M.C., Sanders, G.H.W., Tendler, S.J.B., and Williams, P.M. (2001). Molecular patterning on carbon based surfaces through photobiotin activation. Analyst *126*, 195-198.

124. Gerhardt, K.E., Wilson, M.I., and Greenberg, B.M. (2005). Ultraviolet wavelength dependence of photomorphological and photosynthetic responses in Brassica napus and Arabidopsis thaliana. Photochemistry and Photobiology *81*, 1061-1068.

125. Holden, M.A., and Cremer, P.S. (2003). Light activated patterning of dye-labeled molecules on surfaces. Journal of the American Chemical Society *125*, 8074-8075.

126. Biasco, A., Pisignano, D., Krebs, B., Pompa, P.P., Persano, L., Cingolani, R., and Rinaldi, R. (2005). Conformation of microcontact-printed proteins by atomic force miroscopy molecular sizing. Langmuir *21*, 5154-5158.

127. Interliggi, K.A., Zeile, W.L., Ciftan-Hens, S.A., McGuire, G.E., Purich, D.L., and Dickinson, R.B. (2007). Guidance of actin filament elongation on filament-binding tracks. Langmuir *23*, 11911-11916.

128. Lee, S.W., Oh, B.K., Sanedrin, R.G., Salaita, K., Fujigaya, T., and Mirkin, C.A. (2006). Biologically active protein nanoarrays generated using parallel dip-pen nanolithography. Advanced Materials *18*, 1133-1136.

129. Huck, W.T.S. (2008). Responsive polymers for nanoscale actuation. Materials Today *11*, 24-32.

130. Ichimura, K., Oh, S.K., and Nakagawa, M. (2000). Light-driven motion of liquids on a photoresponsive surface. Science *288*, 1624-1626.

131. Wischerhoff, E., Uhlig, K., Lankenau, A., Borner, H.G., Laschewsky, A., Duschl, C., and Lutz, J.F. (2008). Controlled cell adhesion on PEG-based switchable surfaces. Angewandte Chemie-International Edition *47*, 5666-5668.

132. Huber, D.L., Manginell, R.P., Samara, M.A., Kim, B.-I., and Bunker, B.C. (2003). Programmed Adsorption and Release of Proteins in a Microfluidic Device. Science *301*, 352-354.

133. Takezawa, T., Mori, Y., and Yoshizato, K. (1990). Cell-Culture on a Thermoresponsive Polymer Surface. Bio-Technology *8*, 854-856.

134. Schmaljohann, D. (2006). Thermo- and pH-responsive polymers in drug delivery. Advanced Drug Delivery Reviews *58*, 1655-1670.

135. Bunker, B.C. (2008). Reversible switching of interfacial interactions. Materials Science & Engineering R-Reports *62*, 157-173.

136. Scarpa, J.S., Mueller, D.D., and Klotz, I.M. (1967). Slow Hydrogen-Deuterium Exchange in a Non-Alpha-Helical Polyamide. Journal of the American Chemical Society *89*, 6024-6030.

137. Heskins, M., and Guillet, J.E. (1968). Solution Properties of Poly(N-isopropylacrylamide). Journal of Macromolecular Science, Part A *2*, 1441-1455.

138. Taylor, L.D., and Cerankowski, L.D. (1975). Preparation of Films Exhibiting a Balanced Temperature-Dependence to Permeation by Aqueous-Solutions - Study of Lower Consolute Behavior. Journal of Polymer Science Part a-Polymer Chemistry *13*, 2551-2570.

139. Schild, H.G. (1992). Poly (N-Isopropylacrylamide) - Experiment, Theory and Application. Progress in Polymer Science *17*, 163-249.

140. Chee, C.K., Rimmer, S., Shaw, D.A., Soutar, I., and Swanson, L. (2001). Manipulating the thermoresponsive behavior of poly(N-isopropylacrylamide). 1. On the conformational behavior of a series of N-isopropylacrylamide - Styrene statistical copolymers. Macromolecules *34*, 7544-7549.

141. Schild, H.G., and Tirrell, D.A. (1991). Microheterogeneous Solutions of Amphiphilic Copolymers of N-Isopropylacrylamide - an Investigation Via Fluorescence Methods. Langmuir *7*, 1319-1324.

142. Winnik, F.M., Ringsdorf, H., and Venzmer, J. (1991). Interactions of Surfactants with Hydrophobically Modified Poly(N-Isopropylacrylamides) .1. Fluorescence Probe Studies. Langmuir *7*, 905-911.

143. Winnik, F.M., Ringsdorf, H., and Venzmer, J. (1991). Interaction of Surfactants with Hydrophobically Modified Poly(N-Isopropylacrylamides) .2. Fluorescence Label Studies. Langmuir *7*, 912-917.

144. Schmaljohann, D., Nitschke, M., Schulze, R., Eing, A., Werner, C., and Eichhorn, Y.J. (2005). In situ study of the thermoresponsive behavior of micropatterned hydrogel films by imaging ellipsometry. Langmuir *21*, 2317-2322.

145. Wu, C., and Zhou, S.Q. (1995). Thermodynamically Stable Globule State of a Single Poly(N-Isopropylacrylamide) Chain in Water. Macromolecules *28*, 5388-5390.

146. Edmondson, S., Osborne, V.L., and Huck, W.T.S. (2004). Polymer brushes via surface-initiated polymerizations. Chemical Society Reviews *33*, 14-22.

147. Pyun, J., Kowalewski, T., and Matyjaszewski, K. (2003). Synthesis of polymer brushes using atom transfer radical polymerization. Macromolecular Rapid Communications *24*, 1043-1059.

148. Balamurugan, S., Mendez, S., Balamurugan, S.S., O'Brien, M.J., and Lopez, G.P. (2003). Thermal response of poly(N-isopropylacrylamide) brushes probed by surface plasmon resonance. Langmuir *19*, 2545-2549.

149. Woodward, N.C., Chowdhry, B.Z., Snowden, M.J., Leharne, S.A., Griffiths, P.C., and Winnington, A.L. (2003). Calorimetric investigation of the influence of cross-linker concentration on the volume phase transition of poly(N-isopropylacrylamide) colloidal microgels. Langmuir *19*, 3202-3211.

150. Prazeres, T.J.V., Santos, A.A., and Martinho, J.M.G. (2004). Adsorption of oligonucleotides on PMMA/PNIPAM core-shell latexes: Polarity of the PNIPAM shell probed by fluorescence. Langmuir *20*, 6834-6840.

151. Ionov, L., Stamm, M., and Diez, S. (2005). Size sorting of protein assemblies using polymeric gradient surfaces. Nano Letters *5*, 1910-1914.

152. Ionov, L., Stamm, M., and Diez, S. (2006). Reversible switching of microtubule motility using thermoresponsive polymer surfaces. Nano Letters *6*, 1982-1987.

153. Ionov, L., Synytska, A., and Diez, S. (2008). Temperature-induced size-control of bioactive surface patterns. Adv Funct Mater *18*, 1501-1508.

154. Reuther, C., Hajdo, L., Tucker, R., Kasprzak, A.A., and Diez, S. (2006). Biotemplated nanopatterning of planar surfaces with molecular motors. Nano Lett *6*, 2177-2183.

155. Thorn, K.S., Ubersax, J.A., and Vale, R.D. (2000). Engineering the processive run length of the kinesin motor. J Cell Biol *151*, 1093-1100.

156. Hunt, A.J., and Howard, J. (1993). Kinesin swivels to permit microtubule movement in any direction. Proc Natl Acad Sci U S A *90*, 11653-11657.

157. Bracewell, R. (1999). In The fourier transform and its applications, 3rd Edition. (New York: McGraw-Hill), pp. 25-50 and 243-244.

158. Thompson, R.E., Larson, D.R., and Webb, W.W. (2002). Precise nanometer localization analysis for individual fluorescent probes. Biophys J *82*, 2775-2783.

159. Toyoshima, Y.Y., Toyoshima, C., and Spudich, J.A. (1989). Bidirectional movement of actin filaments along tracks of myosin heads. Nature *341*, 154-156.

160. Mimori, Y., and Miki-Noumura, T. (1994). ATP-induced sliding of microtubules on tracks of 22S dynein molecules aligned with the same polarity. Cell Motil Cytoskeleton *27*, 180-191.

161. Karabay, A., and Walker, R.A. (1999). Identification of microtubule binding sites in the Ncd tail domain. Biochemistry-Us *38*, 1838-1849.

162. Turner, D., Chang, C., Fang, K., Cuomo, P., and Murphy, D. (1996). Kinesin movement on glutaraldehyde-fixed microtubules. Anal Biochem *242*, 20-25.

163. Sharp, D.J., Rogers, G.C., and Scholey, J.M. (2000). Microtubule motors in mitosis. Nature *407*, 41-47.

164. Gadde, S., and Heald, R. (2004). Mechanisms and molecules of the mitotic spindle. Curr Biol *14*, R797-805.

165. Kwon, M., and Scholey, J.M. (2004). Spindle mechanics and dynamics during mitosis in Drosophila. Trends Cell Biol *14*, 194-205.

166. Fink, G., Hajdo, L., Skowronek, K.J., Reuther, C., Kasprzak, A.A., Diez, S. (2009). The mitotic kinesin-14, Ncd, drives directional microtubule-microtubule sliding. Nature Cell Biology (in press).

167. Sharp, D.J., Rogers, G.C., and Scholey, J.M. (2000). Roles of motor proteins in building microtubule-based structures: a basic principle of cellular design. Biochim Biophys Acta *1496*, 128-141.

168. Burbank, K.S., Mitchison, T.J., and Fisher, D.S. (2007). Slide-and-cluster models for spindle assembly. Curr Biol *17*, 1373-1383.

169. Sharp, D.J., Brown, H.M., Kwon, M., Rogers, G.C., Holland, G., and Scholey, J.M. (2000). Functional coordination of three mitotic motors in Drosophila embryos. Mol Biol Cell *11*, 241-253.

170. Shibahara, M., and Kotake, S. (1998). Quantum molecular dynamics study of light-to-heat absorption mechanism in atomic systems. Int J Heat Mass Tran *41*, 839-849.

171. Mazumdar, M., and Cross, R.A. (1998). Engineering a Lever into the Kinesin Neck. J. Biol. Chem. *273*, 29352-29359.

172. Kawaguchi, K., and Ishiwata, S. (2001). Thermal activation of single kinesin molecules with temperature pulse microscopy. Cell Motil Cytoskel *49*, 41-47.

173. Bohm, K.J., Stracke, R., Baum, M., Zieren, M., and Unger, E. (2000). Effect of temperature on kinesin-driven microtubule gliding and kinesin ATPase activity. Febs Lett *466*, 59-62.

174. Decuevas, M., Tao, T., and Goldstein, L.S.B. (1992). Evidence That the Stalk of Drosophila Kinesin Heavy-Chain Is an Alpha-Helical Coiled Coil. J Cell Biol *116*, 957-965.

175. Lambacher, A., and Fromherz, P. (1996). Fluorescence interference-contrast microscopy on oxidized silicon using a monomolecular dye layer. Appl Phys a-Mater *63*, 207-216.

176. Fujimoto, K., Mizuhara, Y., Tamura, N., and Kawaguchi, H. (1993). Interactions between Thermosensitive Hydrogel Microspheres and Proteins. Journal of Intelligent Material Systems and Structures *4*, 184-189.

177. Duracher, D., Elaissari, A., Mallet, F., and Pichot, C. (2000). Adsorption of modified HIV-1 capsid p24 protein onto thermosensitive and cationic core-shell poly(styrene)-poly(N-isopropylacrylamide) particles. Langmuir *16*, 9002-9008.

178. Vale, R.D., Malik, F., and Brown, D. (1992). Directional Instability of Microtubule Transport in the Presence of Kinesin and Dynein, 2 Opposite Polarity Motor Proteins. Journal of Cell Biology *119*, 1589-1596.

179. Toba, S., Watanabe, T.M., Yamaguchi-Okimoto, L., Toyoshima, Y.Y., and Higuchi, H. (2006). Overlapping hand-over-hand mechanism of single molecular motility of cytoplasmic dynein. Proc Natl Acad Sci U S A *103*, 5741-5745.

180. Hyman, A.A. (1991). Preparation of Marked Microtubules for the Assay of the Polarity of Microtubule-Based Motors by Fluorescence. Journal of Cell Science, 125-127.

181. Rogers, K.R., Weiss, S., Crevel, I., Brophy, P.J., Geeves, M., and Cross, R. (2001). KIF1D is a fast non-processive kinesin that demonstrates novel K-loop-dependent mechanochemistry. Embo Journal *20*, 5101-5113.

182. Papra, A., Gadegaard, N., and Larsen, N.B. (2001). Characterization of ultrathin poly(ethylene glycol) monolayers on silicon substrates. Langmuir *17*, 1457-1460.

Acknowledgements

At this point I am taking the opportunity to express my gratitude to all the people, who supported and contributed to this work in one or the other way.

When I took the chance to work with Dr. Stefan Diez almost 5 years ago I was convinced that he would be an ideal person to supervise my work. And indeed, his easy but determined way as well as his enthusiasm was very often encouraging. Stefan was always open for questions and discussions, and his critical and profound comments improved my abilities in presenting results a lot. However, I am in particular thankful for the freedom and support I experienced in developing my project as well as in managing work and family.

Prof. Dr. Wolfgang Pompe and Prof. Dr. Jonathon Howard were co-supervising my work. Their experienced advise and feedback guided me on the right track and let me come along with my project.

One essential part of the work was the application of different motor constructs. Therefore, I am indebted to the people who expressed and purified them. I thank Dr. D. Drechsel and R. Lemaitre for the biotinylated kinesin (the plasmid was kindly provided by Dr. T. Surrey and Prof. Dr. J. Gelles), Dr. Lukasz Hajdo and Prof. Dr. A.A. Kasprzak (Nencki Institute of Experimental Biology, Warsaw, Poland) for the His6-EGFP-ncd (Dr. K. Skowronek kindly provided the plasmid), and Prof. Dr. P. Satir and Dr. Y. Wada (Albert Einstein College of Medicine, Yeshiva University, New York, USA) for the 22S dynein.

New possibilities were opened for the photothermal patterning approach when Dr. S. Braun and P. Gawlitza (Fraunhofer Institute for Material and Beam Technology (IWS), Dresden, Germany) coated coverslips with thin carbon and silicon layers.

Dr. Andreas Wilde (Fraunhofer Institute for Integrated Circuits (IIS), Division Design Automation (EAS), Dresden, Germany) was a great help in getting the finite element modeling off the ground. He advised me the use of the COMSOL software and assisted in setting up an initial simulation file.

Franziska Friedrich has created most of the schematic three-dimensional illustrations of experimental assays used in my work.

I also want to acknowledge Rob Tucker (Department of Material Science and Engineering, University of Florida, Gainesville, USA) with whom I actually never worked together in the lab. He started both of my projects, the biotemplated patterning as a summer student before I had started my PhD work as well as the photothermal patterning as a Fulbright fellow during my maternity leave.

All current and former members of the research group of Dr. Stefan Diez contributed to the great working conditions and the friendly work climate I experienced. Especially I thank Corina Braeuer who not only expressed and purified the kinesin-1 constructs but also eased my experimental work with other technical and organizational support. Not to forget many coffee breaks that often cheered my up. Till Korten was always being very helpful, especially for resolving problems I encountered with the automated peltier control from Metamorph, which he set up together with the temperature stage. It was also him who helped to improve this work by critically reading and commenting on the manuscript. Further, Dr. Leonid Ionov prepared the PNIPAM layers and Felix Ruhnow did a great job in advising me his excellent tracking software. Bert Nitzsche eased the way for handing in the thesis with respect to several organizational issues. And last but not least, I would like to thank Dr. Jacob Kerssemakers, Dr. Jonne Helenius and Dr. Cecile Leduc for many fruitful discussions especially in the beginning of my work.

Stefan, Lioba and my mother were an important balance to my work. They not only supported me a lot but also let me see the work from another perspective.